Doctoral Dissertation

Gold Nanoparticles Synthesis using Microchip Laser Ablation in Liquids

マイクロチップレーザーを用いた液中レーザーアブレーション
による金ナノ粒子の合成

Hettiarachchi Barana Sandakelum

March 2025

Graduate School of Engineering

Osaka University

Table of content

General Introduction

Metal nanoparticles

Humans have been taking advantage of metal nanoparticles (NPs) since ancient times, with some of the earliest known examples coming from the Roman Era. The Lycurgus Cup, a Roman glass artifact from the 4th century AD [1,2], is a notable example of metal NPs producing a remarkable optical dichroism property. When illuminated from the front, the cup appears green, but it turns red when lit from the back due to the interaction of light with the embedded gold and silver NPs. This historical finding serves as remarkable evidence of the unique properties of metal NPs and their potential applications. Since the time of the Lycurgus Cup, the field of NPs has experienced extraordinary growth. Metal NPs, which typically range from 1 to 100 nanometers in size, exhibit unique physicochemical properties that are distinct from those of their bulk material counterparts [3]. These properties include a high surface area to volume ratio, quantum effects, and surface plasmon resonance (SPR).

The high surface area to volume ratio is particularly significant, as it provides a larger reactive surface area, dramatically improving catalytic efficiency [4]. This makes NPs invaluable in catalysis, where smaller NPs enhance chemical reactions due to their increased surface area. Moreover, the quantum effects in NPs arise from their extremely small size, which leads to discrete energy levels and quantum confinement. The quantum effects of NPs contribute to their unique optical and electronic properties, where their size-dependent properties can be harnessed to the development of nanoscale devices and sensors [5]. The surface plasmon resonance SPR, especially for gold NPs, is another unique characteristic that has profound implications in various fields. SPR is the collective oscillation of electrons in response to light, resulting in strong absorption and scattering properties [6]. This phenomenon is exploited in biomedical applications, such as developing compassionate diagnostic tools and targeted drug delivery systems. For instance, gold nanoparticles (Au NPs) can be functionalized with specific biomolecules to target cancer cells, allowing for precise delivery of therapeutic agents and minimizing damage to healthy tissues [7]. These properties of NPs heavily depend on the physicochemical parameters, which is crucial for their application in various fields. However, achieving NPs with controlled properties has been a significant challenge in each synthesis method, as each method has its own advantages and disadvantages.

Metal nanoparticles preparation

NP fabrication techniques are typically divided into two primary categories: top-down and bottom-up approaches. The top-down approach involves the reduction of bulk materials into nanoscale particles through processes such as sputtering [8], mechanical milling [9], and thermal evaporation [10]. Each of these methods has its own features, for example, Sputtering: This technique involves ejecting material from a target by bombarding it with high-energy particles. Sputtering can produce very pure NPs and can be used for various materials, but it requires sophisticated equipment and can be costly (Figure 1).

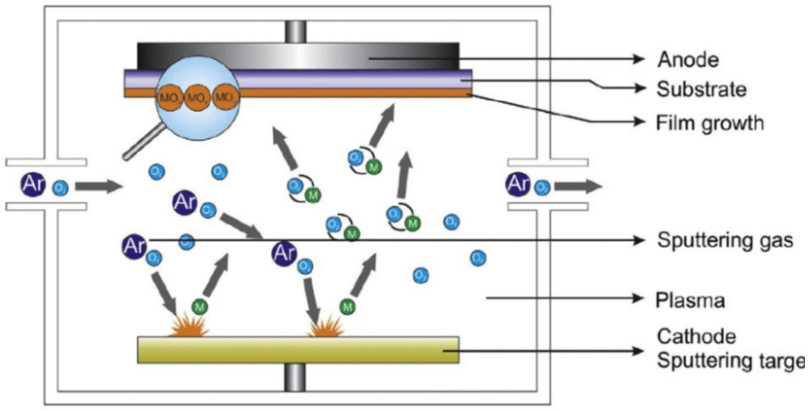

Figure 1. Schematic diagram of sputtering method and process for NP formation.

Mechanical Milling: This method reduces bulk materials into NPs through high-energy collisions among the material particles. It is a relatively simple and cost-effective process that can be used for a wide range of materials. However, it often produces particles with a broad size distribution and can introduce impurities from the milling media (Figure 2).

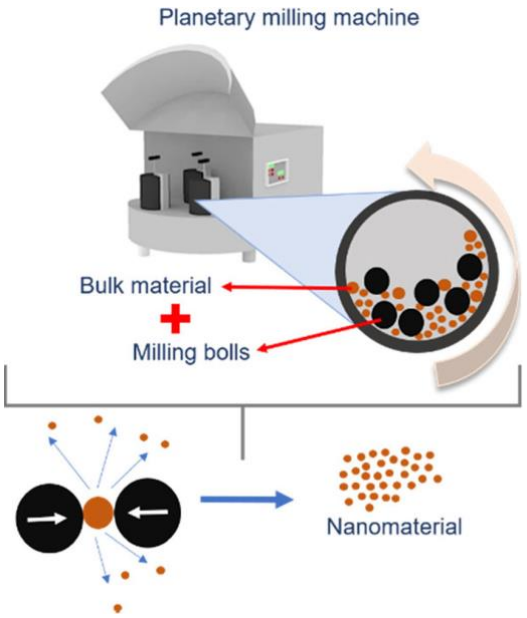

Figure 2. Schematic diagram of mechanical milling method and process for NP formation.

Thermal Evaporation: In this process, bulk materials are vaporized at high temperatures and then condensed into NPs. This method allows the production of high-purity NPs and is suitable for materials with low vapor pressures. However, it requires precise control of temperature and pressure, making it less practical for large-scale production. Conversely, bottom-up methods construct NPs by assembling atomic or molecular components, typically through chemical synthesis techniques such as sol-gel processes [11], co-precipitation [12], chemical vapor deposition [13], and

hydrothermal methods [14]. Sol-Gel Processes: This technique involves the transition of a solution system from a liquid "sol" into a solid "gel" phase. It allows precise control over the composition and structure of NPs and can be performed at relatively low temperatures. However, it can be time-consuming and requires careful control of experimental conditions (Figure 3). Co-precipitation: This method involves the simultaneous precipitation of multiple components from a solution, leading to NPs forming. It is straightforward and cost-effective, suitable for large-scale production. However, it can produce particles with varying sizes and shapes and often requires post-synthesis processing to achieve desired properties.

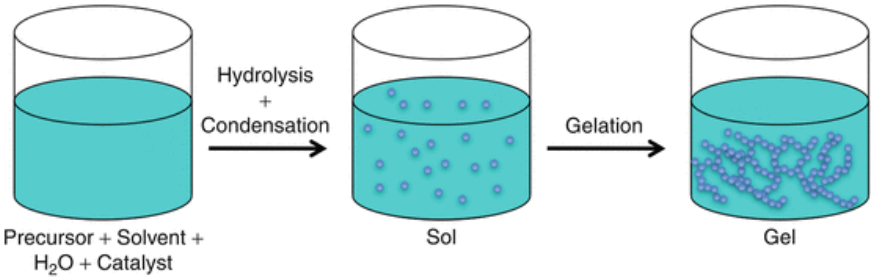

Figure 3. Schematic diagram of the sol-gel processes.

Chemical Vapor Deposition (CVD): CVD involves the deposition of a solid material from a vapor phase onto a substrate, forming NPs. It offers excellent control over particle size and purity and can produce high-quality materials. However, it requires high temperatures and specialized equipment, making it more expensive and less versatile for different materials. Hydrothermal Method: This technique uses high-temperature aqueous solutions under high pressures to grow NPs. It allows for the synthesis of NPs with uniform size and shape and can be used for materials that are otherwise difficult to process. However, it requires high-pressure equipment and can be energy-intensive (Figure 4). Laser ablation, commonly classified as a top-down method due to its use of laser energy to ablate bulk materials and produce NPs, can also be seen as a bottom-up approach. This dual classification is because, after the initial ablation, NPs are formed through nucleation and growth processes of the material components created by the interaction of high-intensity pulsed lasers.

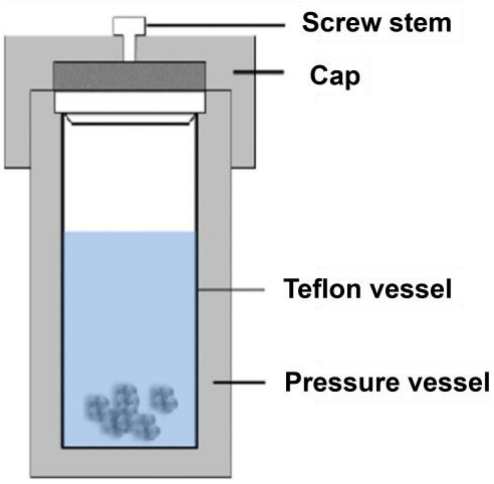

Figure 4. Schematic diagram of the hydrothermal system.

Pulsed laser ablation in liquids

This thesis focuses on pulsed laser ablation in liquid (PLAL), which is an environmentally friendly NP synthesis technique [15-17]. PLAL involves high-energy laser pulses to ablate a bulk solid material submerged in a liquid medium, facilitating the formation of NPs. Notably, PLALs offer unique advantages in synthesizing metal NPs. One of its primary benefits is the high purity of the produced NPs, as the method avoids contamination from external reducing agents. Additionally, PLAL allows for using various solvents, making it a versatile approach to NP synthesis. In the early 1960s, after the advent of the ruby laser, the pioneering use of laser irradiation to ablate materials from a target was first invented [18]. This significant advancement led to the development of pulsed laser ablation for solid materials in laser technology and material science. The first article involving underwater laser ablation for nanomaterial synthesis was conducted by Lida et al. [19]. The material removal and NP formation mechanism in PLALs is characterized by a series of physical and chemical interactions involving the target material, laser, and liquid medium [20,21]. Initially, the laser beam penetrates the liquid (Figure 5A), leading to a rapid phase transition at the target and liquid interface, producing a high-pressure, high-temperature plasma composed of ionized and atomic species originating from the target material (Figure 5B) [22]. This plasma typically persists for durations ranging from several nanoseconds to a few microseconds [23,24], depending on the laser parameters and the surrounding environment [23]. For instance, increasing the laser pulse energy prolongs the plasma's lifetime [23]. As the plasma rapidly cools and decays, the surrounding liquid absorbs the released energy, transforming into a layer of supercritical vapor. This vapor contains the evaporated and dissociated species from the liquid, resulting in the creation of a cavitation bubble (Figure 5B). The laser fluence affects the cavitation bubble's lifetime, and it is known that productivity increases linearly with laser fluence [25.26]. It can be inferred that the bubble's lifetime is directly proportional to the amount of heat available to vaporize a given volume of liquid [26]. At a constant laser fluence, the volume of the bubble further varies depending on the liquid's density and compressibility [27,28], potentially decreasing with higher density and increasing with greater compressibility. Then, the cavitation bubble expands as the plasma is quenched, releasing the ablated material into it (Figure 5C). When the cavitation bubble collapses (Figure 5D), it releases ablated particles into the liquid, generating persistent bubbles (Figure 5E). These persistent bubbles last for several seconds, potentially diffracting the incident laser pulse and interfering with the ablation process through scattering [29,30]. Finally, ablated particles grow and aggregate in the liquid medium (Figure 5F).

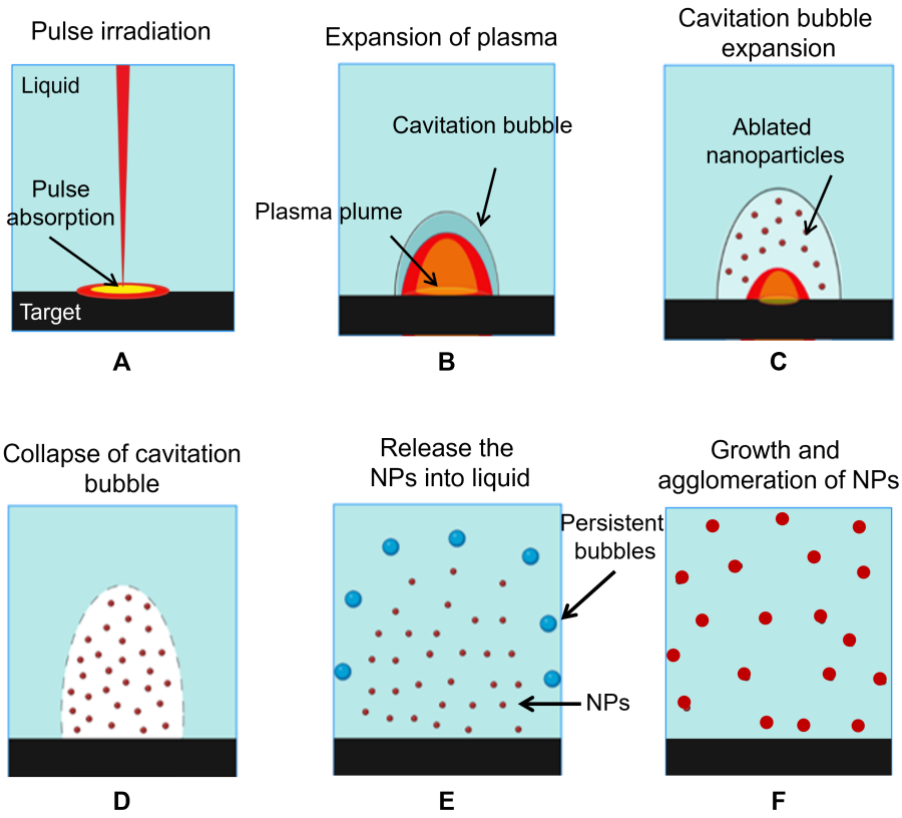

Figure 5. NPs formation mechanism by PLAL.

In the PLAL process, laser parameters significantly influence NP productivity. One crucial parameter is the ablation threshold, which is the minimum energy density required for laser removal of the material. This threshold varies widely depending on the ablated target material [31] and the specific laser parameters. For example, pulse duration is one key factor affecting the ablation threshold; for longer pulse durations (nanoseconds), the threshold fluence depends on the pulse duration as described by Equation 1.

$$F_{th} = \frac{\sqrt{(Kt_p)}\varepsilon_b n_a}{A} \qquad (1)$$

where F_{th} is threshold fluence, t_p is pulse duration, K is coefficient for thermal diffusion, n_a is the number density of atoms in the target, ε_b is the binding energy of ions in the lattice, and A is absorption coefficient. In this case, the duration exceeds the timescales for electron-ion energy transfer, leading to a thermal ablation process. Conversely, for short pulse durations (femtoseconds), the threshold fluence does not depend on the pulse duration, as described by Equation 2.

$$F_{th} = \frac{3}{8}(\varepsilon_b + \varepsilon_{esc})\frac{\lambda n_e}{2\pi} \qquad (2)$$

where ε_{esc} is the work function, n_e is the number density of free electrons, and λ is the laser wavelength. Here, the duration is shorter than the timescales for electron-ion energy

transfer, resulting in a non-thermal ablation process [32]. Meanwhile, the ablation threshold is directly proportional to the laser wavelength, with longer wavelengths typically having higher thresholds due to lower photon energy [32]. The lifetime of the cavitation bubble, which is significantly correlated with productivity, is proportional to the pulse energy and laser fluence [33]. A shorter cavitation bubble lifetime can elevate the applicable repetition rate, thereby enhancing overall NP productivity. At higher pulse repetition rates, the efficiency of the laser is reduced because previously generated cavitation bubbles scatter the laser, covering the target. Therefore, at lower repetition rates all of the laser pulses contribute to the material removal process (Figure 6) [34]. Despite this, increasing the pulse repetition rate can still increase the NP generation, as each pulse generates NPs. This can be optimized by changing the interpulse distance through the scanning speed of the laser beam [34,35].

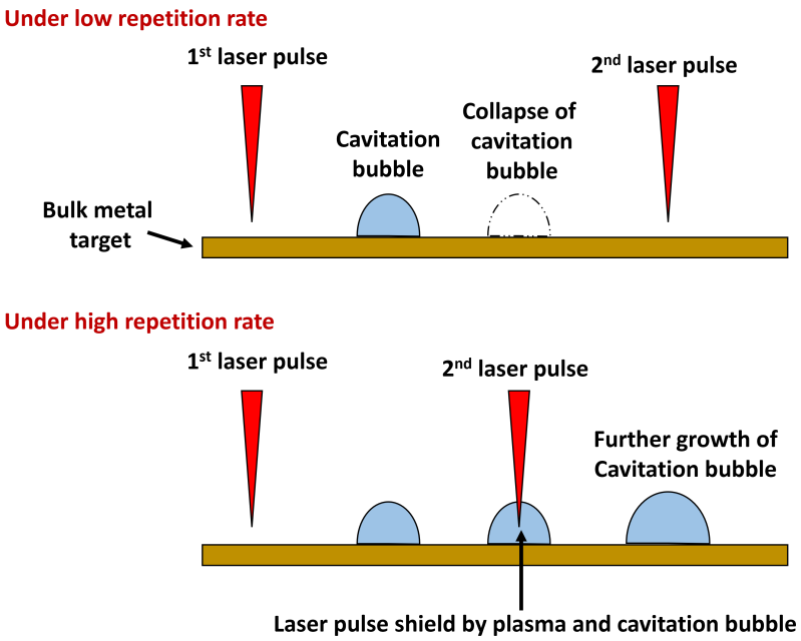

Figure 6. Schematic representation of repetition rate on cavitation bubble.

In addition to these factors, several other aspects influence PLAL productivity, including water breakdown [36], liquid molecule decomposition [37], colloidal shielding [38], and limited optical penetration depth [31]. Optimizing these parameters is crucial for maximizing NP productivity in the PLAL process. Also, these laser parameters highly influence the resulting NP size associated with different phenomena. For instance, NPs with smaller sizes and narrow size distribution can also be achieved by increasing the laser fluence [39,40] due to the in-situ laser-induced fragmentation, where NPs absorb energy and break down into smaller particles during the laser ablation process (Figure 7) [41]. When the energy is above the fragmentation threshold, the particles evaporate, producing smaller particles and significantly reducing the NP size; in contrast, when the laser energy is above the melting energy threshold but below the fragmentation threshold, particle melting occurs, and the NP

size increases [16]. This laser-induced fragmentation is also associated with laser wavelength. Shorter wavelengths, such as 532 nm and 355 nm lasers, tend to generate smaller NPs under the same pulse duration due to increased self-absorption-induced fragmentation [42,43]. In addition to the laser fluence and wavelength, the degree of size reduction by laser-induced fragmentation is influenced by the irradiation period, focal length, beam diameter, and the number of pulses. Typically, higher laser fluence and longer irradiation times produce much smaller particles [44]. Furthermore, the formation of different sizes of NPs during PLAL is attributed to several factors, including the thermal heating of the target by plasma and mechanical erosion induced by cavitation bubbles [45]. Another report identified thermal vaporization and explosive boiling of ablated target surface as key mechanisms behind the different size distributions [46]. Additionally, the beam intensity distribution across the target surface varies with different excitation regimes and their corresponding thresholds [47]. The central spot of the laser beam, with the highest fluence, is defined as the ablation area, while the surrounding lower-fluence ring corresponds to the annealing area, and the outermost zone is the modification area. These distinct regions exhibit varying ablated mass densities, affecting the nucleation and growth of NPs and ultimately leading to the formation of NPs of different sizes [47].

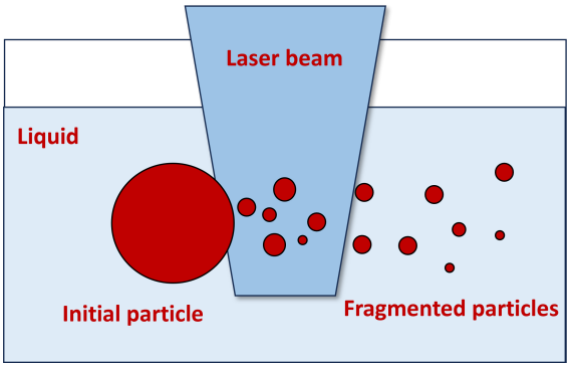

Figure 7. Schematic representation of laser-induced fragmentation process

Table 1. Influential factors on NP productivity and particle size

	Influential factors	**Controlling parameters**
Nanoparticle productivity	Ablation threshold	Type of target Pulse duration Laser wavelength
	Cavitation bubble lifetime	Pulse duration Pulse energy Solution viscosity
	Laser bean shielding	Repetition rate Persistent gas bubble Ablated NPs
Nanoparticle size	Laser-induced fragmentation	Laser fluence Laser wavelength Irradiation period Focal length Beam diameter Number of pulses
	Laser beam intensity distribution	Laser fluence Pulse duration Beam spot size Repetition rate
	Surface stabilization	Surfactant/polymer/biomolecule concentration Solvent polarity/functional groups

In addition to laser parameters, the physical properties of the surrounding media also influence the ablation mechanism. For instance, the density of the surrounding media affects cavitation bubble growth and collapse, which is dominated by inertial forces [48]. Also, in highly viscous liquids, the transport of NPs and the persistence of bubbles within this interface layer are strongly diffusion-controlled [49]. Moreover, solvents with low vaporization enthalpy lead to decomposition, forming gas bubbles that result in laser pulse shielding effects, subsequently decreasing the laser ablation efficiency [50]. Various substances, including surfactants, electrolytes, polymers, biomolecules, and organic solvents, are employed to regulate NP size during laser ablation. Surfactant molecules like CTAB [51] and SDS [52,53] can terminate the growth of embryonic particles, with increasing concentrations generally resulting in smaller NPs. Steric stabilization with biomolecules or polymers occurs through physisorption onto ablated NP surfaces via van der Waals interactions. Polymers effectively apply size-quenching effects, and functionalized polymer end groups, such as thioether and thiols, allow for chemisorption on growing particles, which is more efficient in producing

smaller NPs [54-56]. Organic solvents play multiple roles in size quenching and particle stabilization. These solvents decompose during laser ablation, and the newly formed molecules may quench NP growth [57] or react with ablated matter to create new nanostructures [58]. Solvent molecules with surface affinity functional groups, such as thiols and ketones, and the solvent's polarity stabilize ablated NPs [59,60]. As shown in Table 1, the combined effects of laser parameters and the properties of the surrounding solution media, including surfactant or polymer, on NP size control and productivity involve multiple interacting factors. This highlights the necessity for a more thorough understanding to optimize the PLAL process, thereby achieving optimal results in both size control and productivity.

Microchip laser

In the late 1980s, the advent of high-power, high-efficiency, and high-temperature laser diodes and laser diode arrays marked a transformative period for solid-state lasers [61]. Particularly, the rapid advancements in Nd:YAG (Nd^{3+}:$Y_3Al_5O_{12}$) lasers, driven by AlGaAs active quantum wells emitting at 808 nm, revolutionized the field. These diode laser pump sources, characterized by their narrowband and high spectral brightness, outperformed traditional broadband arc or flash lamps. This technology significantly enhanced the downsizing, efficiency, stability, and longevity of diode-pumped solid-state lasers. The exploration of micro-domain structures and boundary control further enhanced the optical effects, leading to the development of high-brightness microchip solid-state lasers [61]. These compact, high-power density microchip lasers have become indispensable in applications requiring high mobility and peak power, such as laser ignition [62], laser peening [63], laser-induced breakdown spectroscopy [64], and robotic laser material processing [65].

MCLs, with peak powers comparable to femtosecond lasers, can induce plasma in all materials due to their sub-nanosecond pulse duration and single axial mode. This makes them ideal for efficient nonlinear optical processes, balancing high intensity for nonlinearity with long interaction times. The sub-nanosecond pulses also result in high conversion efficiencies for terahertz generation in materials like $LiNbO_3$ and are energy-efficient for air breakdown processes due to their lower breakdown threshold fluence [66].

The development of MCLs has been propelled by the use of quasi-continuous-wave end-pumping and high thermal conductive laser host materials such as YAG, which help mitigate thermal effects. The high damage threshold of YAG necessitates the use of Cr:YAG as a saturable absorber. Notably, almost all MCLs with megawatt-level peak power, based on

pulse energies exceeding 1 mJ and durations less than 1 ns, utilize Cr:YAG with an initial transmittance of around 30% [67].

Professor Taira's development of compact, low-power, giant-pulse MCLs represents a significant milestone (Figure 8). The microchip lasers presented in this thesis feature a monolithic Nd:YAG/Cr^{4+}:YAG ceramic with dimensions of 3 × 3 × 10 mm^3, Nd-doping rate of 1.1 at.%, and 30% initial transmittance of Cr^{4+}:YAG [68-72]. These lasers, housed in a metal module with dual-coated input surfaces for anti-reflection at 808 nm and high-reflection at 1064 nm and output surfaces with 50% partial reflection coating, generate laser pulses with peak powers exceeding 0.5 MW at 100 Hz and a wavelength of 1064 nm without active cooling.

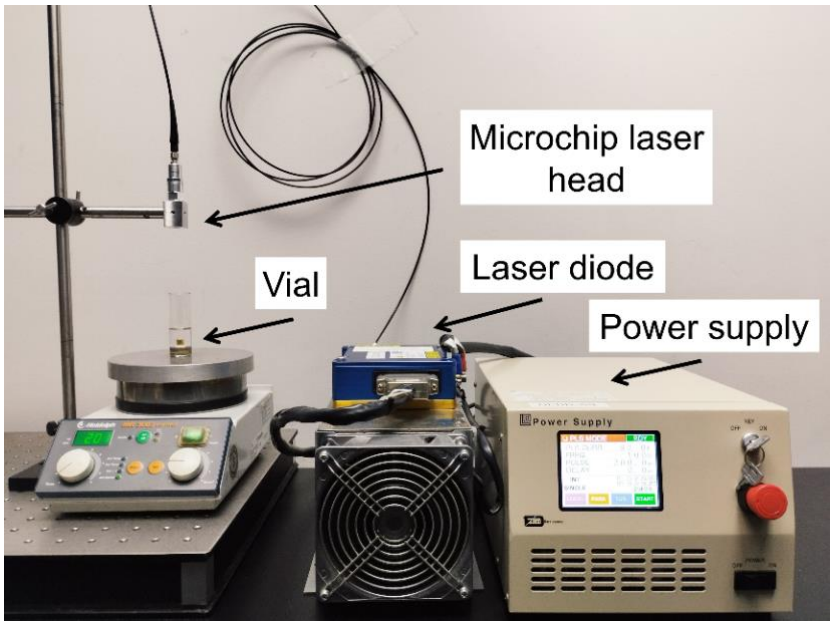

Figure 8. Components of microchip laser system.

MCLs offer several advantages:

- **Compactness and Portability**: The small size of MCL systems enhances their portability and reduces the space required for operation.
- **Ease of Use**: The cavity-coated monolithic structure of MCLs eliminates the need for strict optical system alignment, simplifying both their use and maintenance.
- **Low pulse energy and repetition rate**: Enables the use of highly volatile organic solvents.
- **Short pulse duration**: Reduce the laser energy loss and enhance the efficiency and effectiveness of MCLs [38,73,74].

These features make MCLs a versatile and user-friendly solution for various applications. In catalytic chemistry labs, for example, MCLs enable colloidal NPs' easy and rapid production. This innovation paves the way for the broader adoption of laser techniques in scientific research, breaking down barriers for non-specialists and fostering more significant advancements in the field. Thus, this study comprehensively investigates the preparation of Au NPs through PLAL using MCLs in both aqueous and organic solutions. It examines how MCL laser parameters and solvent properties affect particle size and NP productivity. Additionally, it explores the underlying ablation mechanisms of this innovative MCL system. The findings from this research are expected to contribute to advancements in laser technology and material science, providing insights into optimizing laser parameters for innovative laser development and efficient NP production.

Thesis Outline

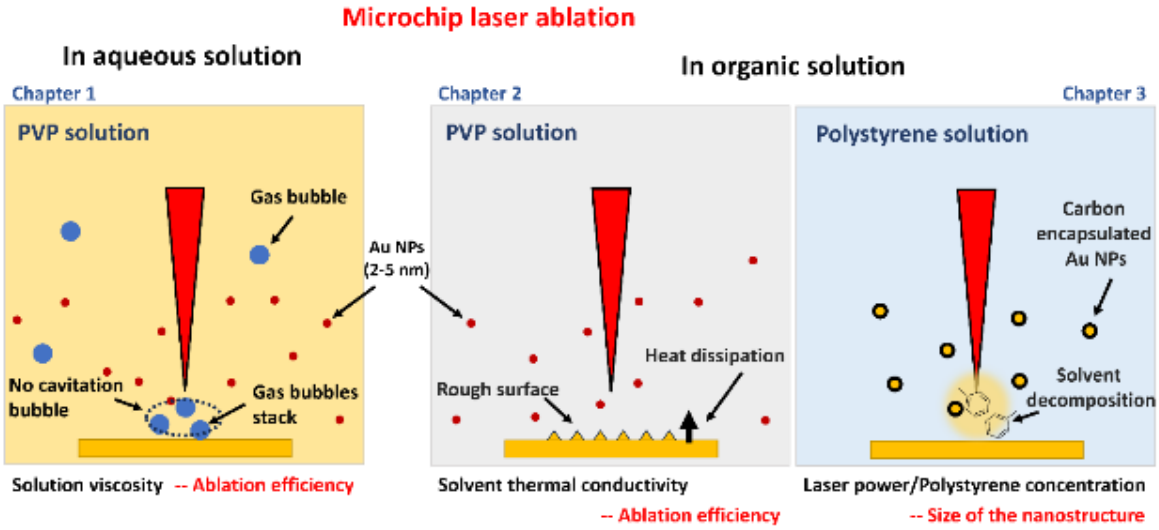

Figure 9. Summary of microchip laser ablation in liquids.

In this doctoral thesis, the author investigates the use of a microchip laser with a short pulse duration of 0.9 ns and a low repetition rate of 100 Hz for PLAL of bulk gold in both aqueous and organic media. Chapter 1 focuses on the effects of laser specifications, particularly examining solution viscosity, which is controlled by the concentration and chain length of poly(*N*-vinyl-2-pyrrolidone) (PVP). The generated Au NPs with a relatively small particle size of 2-5 nm are likely due to the significantly small cavitation bubble created by the low pulse energy and small spot size. The yield of NPs was notably influenced by the solution viscosity, which affects gas bubble diffusion and, consequently, the laser energy transfer to the system. Despite the low repetition rate resulting in a smaller yield of AuNPs, the short 0.9 ns pulse duration mitigated the energy shielding effect, enabling relatively high ablation efficiency even with much lower pulse energy compared to other systems.

Chapter 2 presents a comprehensive study on the preparation of Au NPs within various organic solvents commonly used in organic synthesis, including CH_2Cl_2, $CHCl_3$, 2-PrOH, MeCN, DMF, EtOH, NMP, and DMSO. Using PVP as a stabilizing agent, this chapter examines how different organic solvents affect the size of Au NPs and their ablation efficiency. The experimental setup employed low pulse energy, and due to the thermal conductivity of the solvents, multiple laser pulses were necessary to successfully produce Au NPs. This phenomenon, known as the 'incubation effect,' underscores the importance of considering both experimental parameters and solvent characteristics for the precise synthesis of NPs.

Chapter 3 presents an innovative method for preparing carbon-encapsulated Au nanostructures using PLAL with the MCL system. In this approach, polystyrene is used as a stabilizing agent, and toluene serves as the carbon source, allowing precise control over the size of the nanostructures and the thickness of the carbon layer. The study reveals that the concentration of polystyrene significantly influences both the Au size and the carbon layer thickness. Specifically, using lower laser power and higher polystyrene concentration results in smaller-size Au nanostructures with thinner carbon layers, demonstrating the effectiveness of this technique. The synthesized nanostructures exhibit enhanced photoluminescence properties, which are dependent on the excitation wavelength and carbon layer thickness. This study highlights the potential applications and benefits of using MCL-based PLAL techniques.

References

1. F. Dekker, A. Bunschoten, G. J. Smales, B. R. Pauw, A. H. Velders, V. Saggiomo, *Beilstein J. Nanotechnol.*, **2020**, *11*, 16-23.
2. I. Freestone, N. Meeks, M. Sax, C. Higgitt, *Gold Bull.*, **2007**, *40*, 270-277.
3. O. Salata, *J. Nanobiotechnol*., **2004**, *2*, 3.
4. L. R. Karadaghi, E. M. Williamson, A. T. To, A. P. Forsberg, K. D. Crans, C. L. Perkins, S. C. Hayden, N. J. LiBretto, F. G. Baddour, D. A. Ruddy, N. Malmstadt, S. E. Habas, R. L. Brutchey, *J. Am. Chem. Soc*., **2024**, *146*, 14246-14259.
5. K. Ai, B. Zhang, L. Lu, *Angew. Chemie*., **2009**, *121*, 310-314.
6. G. A. Lopez, M. C. Estevez, M. Soler, L. M. Lechuga, *Nanophotonics*, **2017**, *6*, 123-136.
7. K. P. Tamarov, L. A. Osminkina, S. V. Zinovyev, K. A. Maximova, J. V. Kargina, M. B. Gongalsky, Y. Ryabchikov, A. Al-Kattan, A. P. Sviridov, M. Sentis, *Sci. Rep*., **2014**, *4*, 7034.
8. T. N. Mai, D. Lianlian, Y. Tetsu, *Soft Matter*., **2022**, *18*, 47.
9. X. Wei, X. Wang, B. Gao, W. Zou, L. Dong, *ACS Omega*, **2020**, *5*, 5748-5755.
10. Z. W. Pan, Z. R. Dai, L. Xu, S. T. Lee, Z. L. Wang, *J. Phys. Chem. B*, **2001**, *105*, 2507-2514.
11. J. D. Mackenzie, E. P. Bescher, *Acc. Chem. Res*., **2007**, *40*, 810-818.
12. T. Ahn, J. H. Kim, H. M. Yang, J. W. Lee, J. D. Kim, *J. Phys. Chem. C*, **2012**, *116*, 6069-6076.
13. T. Cheng, K. V. Bets, B. I. Yakobson, *J. Am. Chem. Soc*., **2024**, *146*, 9318-9325.
14. K. K. Somashekharappa, S. V. Lokesh, *ACS Omega*, **2021**, *6*, 7248-7256.
15. D. Zhang, Z. Li, K. Sugioka, *J. Phys Photonics*, **2021**, *3*, 042002.
16. D. Zhang, B. Gökce, S. Barcikowski, *Chem. Rev.*, **2017**, *117*, 3990-4103.
17. M. Kim, S. Osone, T. Kim, H. Higashi, T. Seto, *Kona Powder Part. J.*, **2017**, *34*, 80-90.
18. H. M. Smith, A. F. Turner, *Applied Optics*, **1965**, *4*, 147.
19. Y. Lida, A. Tsuge, Y. Uwanimo, H. Morikawa, T. Ishizuka, *J. A. At. Spectrom*, **1991**, *6*, 7.
20. B. Barcikowski, S. Amendola, V. Lau, M. Marzun, G. Rehbock, C. Reichenberger, S. Zhang, D. Gökce, *Handbook of Laser Synthesis & Processing of Colloids*, Duisburg-Essen Publication Online, **2019**.

21. K. Chaudhary, S. Z. H. Rizvi, J. Ali, Laser-Induced Plasma and its Applications, *Plasma Science and Technology - Progress in Physical States and Chemical Reactions*, InTech, **2016**.
22. T. Sakka, S. Iwanaga, Y. H. Ogata, A. Matsunawa, T. J. Takemoto, *Chem. Phys*., **2000**, *112*, 8645-8653.
23. K. K. Kim, M. Roy, H. Kwon, J. K. Song, S. M. Park, *J. Appl. Phys*., **2015**, *117*, 074302.
24. J. Lam, D. Amans, F. Chaput, M. Diouf, G. Ledoux, N. Mary, K. Masenelli-Varlot, V. Motto-Ros, C. Dujardin, *Phys. Chem. Chem. Phys*., **2014**, *16*, 963-973.
25. R. Tanabe, T. T. P. Nguyen, T. Sugiura, Y. Ito, *Appl. Surf. Sci*., **2015**, *351*, 327-331.
26. R. Streubel, S. Barcikowski, B. Gökce, *Opt. Lett*., **2016**, *41*, 1486-1489.
27. T. Tsuji, D. H. Thang, Y. Okazaki, M. Nakanishi, Y. Tsuboi, M. Tsuji, *Appl. Surf. Sci*., **2008**, *254*, 5224-5230.
28. A. Menéndez-Manjón, B. N. Chichkov, S. Barcikowski, *J. Phys. Chem. C*, **2010**, *114*, 2499-2504.
29. M. R. Kalus, N. Bärsch, R. Streubel, E. Gökce, S. Barcikowski, B. Gökce, Phys. Chem.Chem. Phys., **2017**, *19*, 7112-7123.
30. M. Brikas, S. Barcikowski, B. Chichkov, G. Raciukaitis, Journal of Laser Micro Nanoengineering, **2007**, *2*, 230-233.
31. P. T. Mannion, J. Magee, E. Coyne, G. M. O'Connor, T. Glynn, *J. Appl. Surf. Sci*., **2004**, *233*, 275-287.
32. E. G. Gamaly, A. V. Rode, B. Luther-Davies, V. T. Tikhonchuk, *Phys. Plasmas*, **2002**, 9, 949-957.
33. S. Reich, P. Schönfeld, A. Letzel, S. Kohsakowski, M. Olbinado, B. Gökce, S. Barcikowski, A. Plech, *ChemPhysChem*., **2017**, *18*, 1084.
34. P. Wagener, A. Schwenke, B. N. Chichkov, S. Barcikowski, *J. Phys. Chem. C*, **2010**, *114*, 7618-7625.
35. O. V. Overschelde, J. Dervaux, L. Yonge, D. Thiry, R. Snyders, *Laser Phys*., **2013**, *23*, 055901.
36. G. Cristoforetti, E. Pitzalis, R. Spiniello, R. Ishak, M. Muniz- Miranda, *J. Phys. Chem. C*, **2010**, *115*, 5073-5083.
37. H. Zhang, C. Liang, J. Liu, Z. Tian, G. Shao, *Carbon*, **2013**, *55*, 108-115.
38. S. Dittrich, R. Streubel, C. McDonnell, H. P. Huber, S. Barcikowski, B. Gokce, *Appl. Phys. A*, **2019**, *125*, 432.

39. E. Solati, L. Dejam, D. Dorranian, *Opt. Laser Technol*., **2014**, *58*, 26-32.
40. Y.-H. Chen, C.-S. Yeh, *Colloids Surf., A*, **2002**, *197*, 133-139.
41. R. Intartaglia, K. Bagga, F. Brandi, *Opt. Express*, **2014**, *22*, 3117-3127.
42. A. Hamad, L. Li, Z. A. Liu, *Appl. Phys. A: Mater. Sci. Process*., **2015**, *120*, 1247-1260.
43. E. Akman, B. G. Oztoprak, M. Gunes, E. Kacar, A. Demir, *Photonics Nanostruct*., **2011**, *9*, 276-286.
44. V. Amendola, M. Meneghetti, *J. Mater. Chem*., **2007**, *17*, 4705-4710.
45. J. P. Sylvestre, A. V. Kabashin, E. Sacher, M. Meunier, *Appl. Phys. A: Mater. Sci. Process*., **2005**, *80*, 753-758.
46. W. T. Nichols, T. Sasaki, N. Koshizaki, *J. Appl. Phys*., **2006**, *100*, 114912.
47. J. Bonse, S. Baudach, J. Krüger, W. Kautek, M. Lenzner, *Appl. Phys. A: Mater. Sci. Process*., **2002**, *74*, 19-25.
48. J. Long, M. H. Eliceiri, L. Wang, Z. Vangelatos, Y. Ouyang, X. Xie, Y. Zhang C. P. Grigoropoulos, *Opt. Laser Technol*., **2021**, *134*, 106647.
49. M.-R. Kalus, R. Lanyumba, S. Barcikowski, B. Gokce, *J. Flow Chem*., **2021**, *11*, 773-792.
50. T. Fromme, L. K. Tintrop, S. Reichenberger, T. C. Schmidt, S. Barcikowski, *ChemPhysChem*., **2023**, *24*, e202300089.
51. M. A. Sobhan, M. J. Withford, E. M. Goldys, *Langmuir*, **2009**, *26*, 3156-3159.
52. F. Mafuné, J.-Y. Kohno, Y. Takeda, T. Kondow, H. Sawabe, *J. Phys. Chem. B*, **2000**, *104*, 9111-9117.
53. F. Mafuné, J.-Y. Kohno, Y. Takeda, T. Kondow, *J. Phys. Chem. B*, **2002**, *106*, 7575-7577.
54. S. Besner, A. V. Kabashin, F. M. Winnik, M. Meunier, *J. Phys. Chem. C*, **2009**, *113*, 9526-9531.
55. K. Habiba, D. P. Bracho-Rincon, J. A. Gonzalez-Feliciano, J.C Villalobos-Santos, V. I. Makarov, D. Ortiz, J. A. Avalos, C. I. Gonzalez, B. R. Weiner, G. Morell, *Appl. Mater. Today*, **2015**, *1*, 80-87.
56. V. Nguyen, L. Yan, J. Si, X. Hou, *Opt. Mater. Express*, **2016**, *6*, 312-320.
57. P. V. Kazakevich, V. V. Voronov, A. V. Simakin, G. A. Shafeev, *Quantum Electron*, **2004**, *34*, 951-956.
58. T. Tsuji, T. Hamagami, T. Kawamura, J. Yamaki, M. Tsuji, *Appl. Surf. Sci*., **2005**, *243*, 214-219.
59. M. Kawasaki, *J. Phys. Chem. C*, **2011**, *115*, 5165-5173.

60. E. Giorgetti, M. Muniz-Miranda, P. Marsili, D. Scarpellini, *J. Nanopart. Res*., **2012**, *14*, 648.
61. R. L. Byer, *Science*, **1988**, *239*, 742-747.
62. N. Pavel, M. Bärwinkel, P. Heinz, D. Brüggemann, G. Dearden, G. Croitoru, O. V. Grigore, *Prog. Quantum Electron*., **2018**, *58*, 1-32.
63. Y. Sano, K. Masaki, Y. Mizuta, S. Tamaki, T. Hosokai, T. Taira, *Metals*, **2021**, *11*, 1716.
64. K. Tamura, H. Ohba, M. Saeki, T. Taguchi, H. H. Lim, T. Taira, I. Wakaida, *J. Nucl. Sci. Technol*., **2020**, *57*, 1189-1198.
65. K. A. Ghany, H. A. Rafea, M. Newishy, *Int. J. Adv. Manuf. Technol*., **2006**, *28*, 1111-1117.
66. S. Hayashi, K. Nawata, T. Taira, J. Shikata, K. Kawase, H. Minamide, *Sci. Rep*., **2015**, *4*, 5045.
67. J. Dong, K. Ueda, A. Shirakawa, H. Yagi, T. Yanagitani, A. A. Kaminskii, *Opt. Express*, **2007**, *15*, 14516-14523.
68. T. Taira, A. Mukai, Y. Nozawa T. Kobayashi, *Opt. Lett*., **1991**, *16*, 1955-1957.
69. T. Taira, *IEEE J. Sel. Top. Quantum Electron*, **2007**, *13*, 798-809.
70. H. Sakai, H. Kan T. Taira, *Opt. Express*, **2008**, *16*, 19891-19899.
71. T. Taira, *Opt. Mater. Express*, **2011**, *1*, 1040-1050.
72. H. H. Lim, T. Taira, *Opt. Express*, **2022**, *30*, 5151-5158.
73. S. Dittrich, M. Spellauge, S. Barcikowski, H. P. Huber, B. Gokce, *Opto-Electron Adv*., **2022**, *5*, 210053.
74. S. Dittrich, S. Barcikowski, B. Gokce, *Opto-Electron Adv*., **2021**, *4*, 200072.

Chapter 1

Uncovering Gold Nanoparticle Synthesis using a Microchip Laser System through Pulsed Laser Ablation in Aqueous Solution

1-1. Introduction

Pulsed laser ablation in liquid (PLAL) has emerged as a reliable technique for producing metal nanoparticles (NPs) in solution [1,2]. Unlike conventional chemical methods that use metal ions as precursors, PLAL does not require additional chemicals, resulting in high-purity metal NPs. This method is widely used in various scientific and industrial research fields. However, the main challenge for laboratory implementation of PLAL is the introduction and maintenance cost of the laser source for non-specialists in laser science. To make laser techniques more accessible, Taira et al. developed compact, low-power consumption giant-pulse microchip lasers (MCLs) pumped by laser diode (Figure 1a) [3,4]. These MCLs, with a short cavity length of less than 10 mm, are portable and fit in small spaces, making them suitable for standard organic chemistry labs. The monolithic cavity-coated structure of the MCLs eliminates the need for strict optical system alignment, lowering the entry barrier for non-specialists such as chemists and biologists [3]. These features enable the easy and rapid production of colloidal NPs in catalytic chemistry labs, significantly accelerating the discovery of new catalytic reactions.

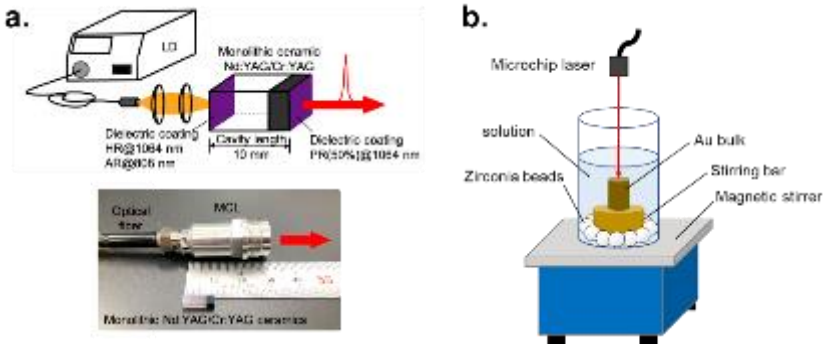

Figure 1. (a) The composition of the MCL system and the scale of the MCL laser head; (b) Setup of the PLAL system in the present research

Recent demonstrations have shown that laser systems with a pulse duration of 1 ns achieve maximum efficiency compared to those with pulse durations of a few ps and >5 ns [5-7]. This efficiency is due to the shielding of the laser beam by the ablation plume and cavitation bubble, which occurs between 1 and 5 ns after the pulse, resulting in minimal losses for PLAL. The MCL system features a short cavity length of less than 10 mm, allowing for minimal pulse

durations of 0.9 ns, expected to achieve optimal PLAL processing. Additionally, the machine operates at a lower repetition rate of 100 Hz. While higher repetition rates can enhance productivity by delivering greater average power [8,9], they may also introduce challenges such as plasma and particle shielding, which can limit laser ablation efficiency [6]. Therefore, evaluating the MCL system's capability for PLAL of metal NPs under short pulse durations (~1 ns) and low repetition rates is crucial. A comprehensive investigation is conducted into the preparation of Au NPs through PLAL using MCLs in an aqueous solution with a short pulse duration and low repetition rate.

This study investigates the preparation of Au NPs using PLAL with MCLs in an aqueous solution, focusing on short pulse durations and low repetition rates. The ablation mechanisms of this innovative MCL system are examined to advance the utilization of MCLs, particularly in chemistry.

1-2. Results and Discussion

MCL ablation in aqueous PVP solution

The investigation began with the PLAL experiment using the MCL system on a gold target in water without any stabilizing surfactant. During ablation, the solution's color changed from colorless to pink, indicating the absorption band of surface plasmon resonance (SPR) at 522 nm. The absorption spectra of the solution were similar to those of Au NPs synthesized by chemical reduction of gold salt and by PLAL with a conventional laser source [10-13], confirming that the present PLAL with the MCL system effectively produced Au NPs. TEM measurement verified the presence of Au NPs, with a particle size of 4.9 ± 1.3 nm (Figure 2).

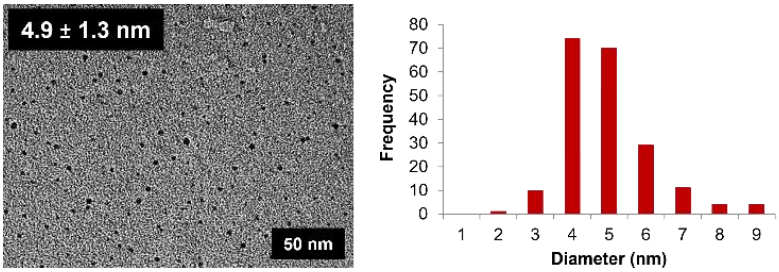

Figure 2. TEM images and size distributions of the Au NPs produced by PLAL using the MCL in water.

As the efficiency of MCL for generating Au NPs was confirmed, the effect of the surfactant PVP was investigated, a polymer-based stabilizing agent for metal nanocolloids that creates a weakly bound colloidal structure via charge transfer interaction between the N−C=O groups and Au [14-16]. The PVP chain length and concentration are known to affect particle size and colloid size when using chemical reduction methods, influencing catalytic ability [17-18]. However, there is no explicit discussion on the relationship between polymer chain length

and particle size when using PLAL. Therefore, PLAL using the MCL system was conducted using the Au target in thePVP solution. To investigate the effect of PVP chain length, three types of PVPs, K-15, K-30, and K-90, with different chain lengths (Mw: 10 kDa, 40 kDa, and 360 kDa, respectively) were used. PLAL was performed with various concentrations of PVP in water. Shortly after ablation began, the PVP solution turned reddish from colorless. TEM measurements of the colloidal solutions showed slightly smaller Au NPs than those obtained without PVP (Table 1). However, particle size remained uniform across all trials, indicating that PVP chain length and concentration were not significant factors for particle size determination.

Table 1. Effects of PVP concentration and chain length on Au NP size

PVP concentration (mol L^{-1})	Particle size (nm)		
	PVP K-15	PVP K-30	PVP K-90
1.0×10^{-4}	4.2 ± 1.4	3.9 ± 1.2	4.3 ± 1.4
1.0×10^{-3}	3.9 ± 1.0	3.5 ± 0.9	3.9 ± 0.6
1.0×10^{-2}	3.7 ± 0.9	3.3 ± 1.0	3.6 ± 0.9
1.0×10^{-1}	3.2 ± 0.7	3.1 ± 0.7	3.5 ± 0.8
1.0	3.8 ± 1.0	3.6 ± 0.8	n.d.

Previous works with conventional laser sources show a clear relationship between Au NP particle size and matrix concentration, such as sodium dodecyl sulfate and β-cyclodextrin [12,19]. Silver NPs prepared with different PVP concentrations also showed differences in particle size compared to those without PVP [20], attributed to improved secondary etching efficiency of the solvent-confined plasma towards the silver plate in the presence of PVP. The differences observed using MCL versus conventional laser methods may be due to differences in laser specifications.

The UV-vis spectra analysis of the colloidal solutions revealed the impact of PVP on PLAL using MCLs (Figure 3). Increased PVP concentrations reduced the absorption intensity of the plasmonic band at 519 nm for all PVP types. The spectral shapes of the SPR bands remained almost identical. Inductively coupled plasma-atomic emission spectroscopy (ICP-AES) measurements confirmed a significant decrease in the yield of Au NPs with higher PVP concentrations, independent of PVP chain length (Table 2). Notably, beyond a PVP concentration of 1.0×10^{-1} mol/L, there was a substantial decline in the quantity of Au NPs produced. To gain deeper insights into the relationship between PVP concentration and the yield of Au NPs, other relevant parameters were investigated, with viscosity being particularly noteworthy. As summarized in Table 2 and Figure 2, the experimental results revealed a distinct correlation between the yield of Au NPs and the viscosity of the reaction solution. To further explore this connection, PLAL experiments were conducted using a solution with a fixed viscosity (~2.2 mPa·s) while varying PVP chain lengths. Interestingly, regardless of the

specific PVP chain length employed, the quantity of ablated Au NPs remained consistent. This result strongly suggests that solution viscosity is pivotal in determining ablation efficiency in the presence of PVP.

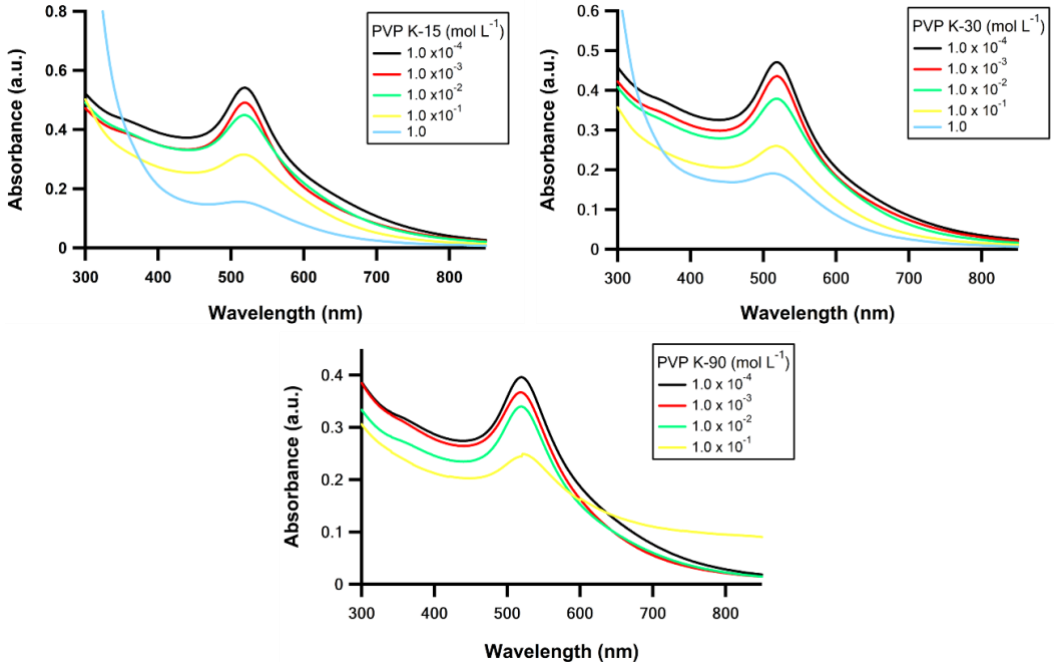

Figure 3. UV/Vis absorption spectrum of Au NPs in different concentrations of PVPs

Table 2. Effects of PVP concentration and chain length on Au NP concentration.

PVP concentration (mol L^{-1})	PVP K-15		PVP K-30		PVP K-90	
	Au productivity (µg h^{-1})	Viscosity (mPa·s)	Au productivity (µg h^{-1})	Viscosity (mPa·s)	Au productivity (µg h^{-1})	Viscosity (mPa·s)
1.0×10^{-4}	226	0.94 ± 0.05	236	0.94 ± 0.02	223	0.95 ± 0.05
1.0×10^{-3}	220	0.94 ± 0.04	200	0.95 ± 0.02	200	0.96 ± 0.01
1.0×10^{-2}	192	0.96 ± 0.04	196	0.96 ± 0.04	131	1.07 ± 0.02
1.0×10^{-1}	179	1.01 ± 0.02	107	1.26 ± 0.06	75	3.27 ± 0.03
1.0	104	2.32 ± 0.03	76	6.39 ± 0.03	n.d	n.d

Real-time monitoring of the ablation in aqueous media

To understand how solution viscosity influences ablation efficiency, PLAL experiments were conducted using a gold target under varying viscosity conditions. Real-time monitoring of the ablation process was achieved using a high-speed camera, capturing images at 4 ms per frame during the initial laser ablation and five minutes after. The results demonstrated the influence of PVP solution viscosity on the initial laser ablation stage during the production of Au NPs (Figure 4). When a low-viscosity PVP K-15 solution underwent laser ablation, Au NPs were ejected and dispersed rapidly, generating only a small amount of gas bubbles (Figure 4A). This

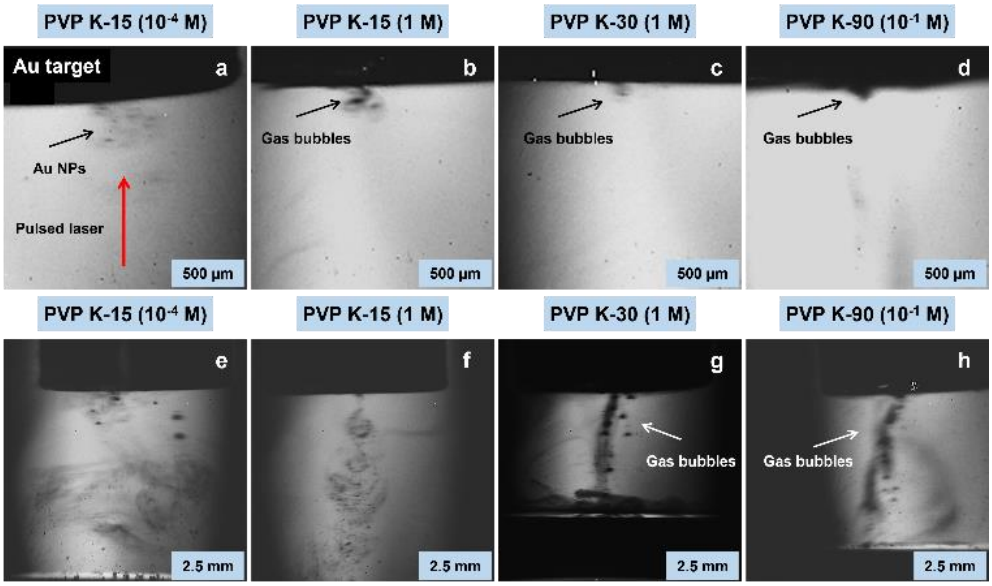

Figure 4. Snapshot images of gas bubbles accumulation on the laser irradiation pathway in PVP aqueous solution with different viscosity.

behavior is due to the high dispersibility of gas bubbles in low-viscosity media. In contrast, as the viscosity increased with a higher viscosity PVP K-15 solution, the ejection rate of NPs decreased, and gas bubble dispersion became less effective (Figure 4B). Under even higher viscosity conditions with PVP K-30 and PVP K-90, both the ejection rate of NPs and the dispersion of gas bubbles became considerably slower, particularly with PVP K-30, which exhibited the highest viscosity (Figures 4C and 4D). Five minutes after laser irradiation, gas bubbles moved slowly through the solution, positioning themselves along the laser pathway in all tested conditions (Figures 4E-4H). This phenomenon hindered the smooth energy transfer from subsequent laser pulses to the target material, as the persistent bubbles acted as a shield. These observations revealed that the solution's viscosity influenced the lifetime of air bubbles, ultimately controlling the effectiveness of the laser ablation process. This phenomenon, known as "the shielding effects" of persistent bubbles, is a recognized occurrence in the general PLAL mechanism. Typically, these persistent bubbles are generated after the collapse of the cavitation bubble during the ablation process. They partially disperse in the solution and adhere to the bulk gold target surface, even after several milliseconds to seconds, particularly in highly viscous media [21-24]. In contrast to conventional laser systems, small gas bubbles formed immediately after laser irradiation at the target surface. They exhibited slow movement along the laser pathway and retained a stable spherical form even after five minutes. These observations suggest that these gas bubbles absorbed, reflected, and scattered the laser beam,

acting as a shield for subsequent laser pulses, similar to the role played by persistent bubbles, thus negatively impacting the efficiency of Au NP ablation.

Investigation of cavitation bubble formation

The cavitation bubble and plasma plume, typically formed after creating a high temperature and pressure region via high-intensity laser pulse irradiation of a solid target [25-27], were not observed in the current images. Despite capturing images at 2 μs intervals over 10 ms, no cavitation bubbles were detected. The size of cavitation bubbles is primarily influenced by laser fluence when the pulse duration is similar, and the second laser pulse does not affect bubble size within a repetition rate range of 10-1000 Hz. Studies indicate that a 1 ns duration and 0.4 J cm^{-2} fluence can form cavitation bubbles. Although the MCL system's laser fluence exceeds 13.7 J cm^{-2}, cavitation bubbles were likely too small to be detected due to the combination of small pulse energy and spot size.

Although studies have examined the effects of PVP presence [28] and viscosity [29], these findings are challenging to apply directly to my results due to significant differences in PVP concentration and viscosity ranges. My results indicate that PVP does not significantly affect cavitation bubble formation, as bubbles were not observed without PVP. Therefore, my work is crucial in revealing the effects of less understood conditions on the ablation phenomenon. According to the Rayleigh-Plesset theory [30,31], small bubbles likely have a short lifetime, providing limited space for the nucleation and growth of NPs, resulting in relatively small and consistent NP sizes [32]. Additionally, the fragmentation of initially larger NPs by sequential laser pulses over the long ablation time (1 hour) might also contribute to the formation of small NPs [33].

Relationship between the ablation efficiency and the solution viscosity in MCL ablation

In low-viscosity solutions, bubbles diffuse and disappear from the initially generated region within a specific time interval (Δt). In high-viscosity solutions, bubble density remains high along the laser pathway within the same Δt due to suppressed diffusion. The ablation efficiency, considering gas bubbles, is modeled using the three-dimensional diffusion equation (1) based on Fick's second law [34].

$$\frac{\partial C}{\partial t} = D\left(\frac{\partial^2 C}{\partial x^2} + \frac{\partial^2 C}{\partial y^2} + \frac{\partial^2 C}{\partial z^2}\right) \qquad (1)$$

C represents the concentration of diffused gas bubbles at time *t* and coordinates *x*, *y*, and *z* from the laser-generated bubble spot. *D* is the diffusion coefficient. The solution to equation (1) is given by equation (2).

$$C(x,y,z,t) = \frac{C_0}{8(\pi D)^{\frac{3}{2}}} \exp\left[\frac{-(x^2+y^2+z^2)}{4Dt}\right] \qquad (2)$$

The initial concentration of gas bubbles at the generation point on the bulk Au surface (x = 0, y = 0, z = 0) is denoted as C_0 at time $t = 0$. For a fixed volume V, the total amount of gas bubbles at a specific area (x, y, z) with volume V at time t can be represented by equation (3).

$$C(x,y,z,t) \cdot V = \frac{C_0 V}{8(\pi D t)^{\frac{3}{2}}} \exp\left[\frac{-(x^2+y^2+z^2)}{4Dt}\right] \qquad (3)$$

The effect of solution viscosity on gas bubbles' diffusion is explained by the Stokes-Einstein relation, which links the diffusion constant D and viscosity η [35].

$$D = k_B T / 6\pi\eta R \qquad (4)$$

In this equation, k_B is the Boltzmann constant, T is the temperature, and R is the gas bubble radius. By rearranging, the equation becomes:

$$C(x,y,z,t) \cdot V = \frac{C_0 V}{8(\pi t k B T / 6\pi\eta R)^{\frac{3}{2}}} \exp\left[\frac{-(x^2+y^2+z^2)}{4tkBT/6\pi\eta R}\right] \qquad (5)$$

Based on the analysis of the video and ICP data, it was assumed that the intensity of scattered light I is directly proportional to the number of gas bubbles. This relationship can be represented as:

$$I \propto C \cdot V \qquad (6)$$

When specific parameters like temperature, refractive index, wavelength of light, bubble velocity, and shape remain constant, equation (5) can be simplified as follows:

$$C(x,y,z,t) \cdot V = a(b\eta)^{\frac{3}{2}} exp[-c\eta] \qquad (7)$$

Here, *a*, *b*, and *c* are constants. The relationship between the intensity of scattered light I and the concentration of gas bubbles at position (x, y, z) after a time interval Δt is given by:

$$I \propto a(b\eta)^{\frac{3}{2}} exp[-c\eta] \qquad (8)$$

The laser power remaining after interacting with a bubble is the difference between the incident laser power P and the power of the scattered light intensity, mathematically expressed as:

$$\text{Remaining laser power} = P \text{ - Scattered light intensity} \qquad (9)$$

The ablation efficiency, which is tied to the total laser power in the system under consistent instrument settings, is influenced by the viscosity of the reaction media, as shown by the above equations. Specifically, with constant parameters like temperature, refractive index, light wavelength, bubble velocity, and shape, the ablation efficiency of Au NPs decreases as solution viscosity increases. This relationship, described by eq. 9, corresponds with the fitted line of the Au amount versus solution viscosity in Figure 5.

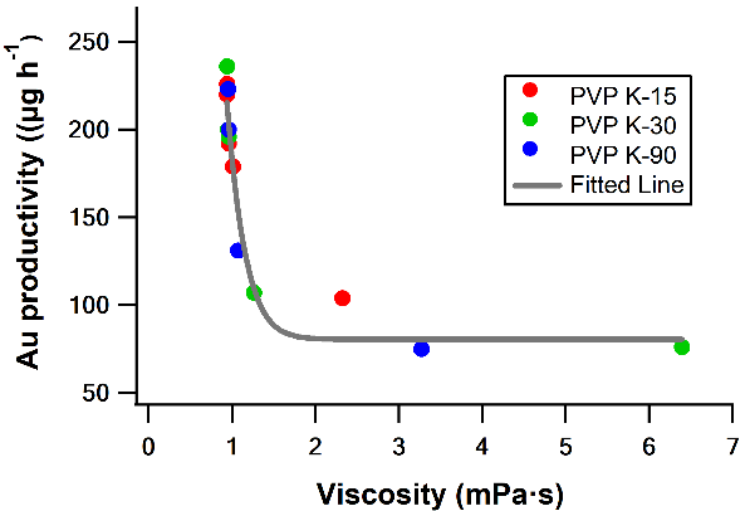

Figure 5. The plot of the ablated Au amount versus solution viscosity. The fitting curve is based on eq. (9).

Perspectives of MCL ablation

The PLAL experiment was conducted to assess the effectiveness of ablation using the MCL system under higher-power laser conditions (Table 3). Due to significant differences in machine specifications, identical pulse energy settings were not feasible. By fixing the total applied laser

Table 3. Settings and PLAL aspects of the present MCL and the ns-laser (Quanta-Ray PRO-250) systems in the comparison experiment.

	Present MCL	Quanta-Ray PRO-250
Pulse energy (mJ)	1.3	25
Pulse duration (ns)	0.9	12
Spot diameter (µm)	130 ± 6	800 ± 13
Repetition rate (Hz)	100	10
Au productivity (µg h^{-1})	101	620
Ablation efficiency (mg W^{-1} h^{-1})	0.8	2.5

power at 100 J and adjusting irradiation times according to the laser spot size (MCL laser for 769 seconds and Quanta-Ray Pro-250 for 400 seconds), distinct outcomes were observed. The MCL system yielded 101 μg/h of Au productivity with an ablation efficiency of 0.8 mg/W·h, compared to 620 μg/h and 2.5 mg/W·h for the Quanta-Ray Pro-250. Despite having approximately 20 times lower pulse energy, the MCL system's high ablation efficiency is attributed to effective energy transfer from each laser shot to the metal surface with a pulse duration of ~1 ns. This avoids energy shielding effects caused by sequential laser plumes, cavitation bubbles, and generated NPs, unlike systems with longer pulse durations. This result highlights the MCL system's potential for environmentally friendly metal NP production with reduced total energy input, promising practical applications in various material fields.

1-3. Conclusions

An experiment was conducted to demonstrate the PLAL of bulk gold in water using an MCL with a short pulse duration of 0.9 ns and a low repetition rate of 100 Hz. The study focused on the impact of laser specifications and solution viscosity, which was controlled by the concentration and chain length of poly(*N*-vinyl-2-pyrrolidone) (PVP). The process produced Au NPs with particle sizes ranging from 2 to 5 nm, likely due to the reduced cavitation bubble size resulting from the low pulse energy and small spot size, although further investigation is needed. The yield of NPs was significantly influenced by solution viscosity, which affects gas bubble diffusion and laser energy transfer. Despite the low repetition rate resulting in a lower yield of Au NPs, the 0.9 ns short pulse duration minimized the energy shielding effect, leading to relatively high ablation efficiency even with smaller pulse energy than other methods. This study provides valuable insights into preparing Au NPs using a compact MCL system and demonstrates the potential for installing an MCL in standard synthetic chemistry laboratories.

1-4. Experimental Section

Materials

All reagents were used without further purification unless specified. Ultrapure water (18.2 Ω cm^{-1}) was produced using an Organo Puric-ω system. Transmission electron microscopy (TEM) images were taken with a JEOL JEM-2100 electron microscope at 200 kV, using a Holey carbon support film-coated Cu microgrid (EMJapan, U1003). The TEM grid underwent hydrophilic treatment in a glow discharge irradiation chamber before use. TEM images were analyzed with Image-J software, with the mean diameter and standard deviation based on an average of 300 particles. Inductively coupled plasma atomic emission spectroscopy (ICP-AES) was performed using Shimadzu ICPS-8100. Viscosity measurements were conducted with a HAAKE RheoStress 6000 (Thermo Scientific) at a shear rate of 1000 s^{-1} and 25 °C. Viscosity values showed no significant variation between pre and post-PLAL, so all measurements were taken before PLAL.

General PLAL method

A gold target (>99.99%, 5 × 15 mm) was cleaned using ultrasonication in acetone for 5 minutes and rinsed with deionized water. The target was mounted on a custom-made PEEK holder with a magnetic stir bar and placed at the bottom of a Pyrex® vessel (30 × 80 mm). Zirconia beads (φ 6 mm) were positioned between the vessel and holder to stabilize the axis of rotation (Figure 1b). Next, 15 mL of an aqueous solution containing poly(*N*-vinyl-2-pyrrolidone) (PVP) (K-15: 10 kDa, K-30: 40 kDa, K-90: 360 kDa) at concentrations of 10^{-4} mol L^{-1}, 10^{-3} mol L^{-1}, 10^{-2} mol L^{-1}, 10^{-1} mol L^{-1}, and 1 mol L^{-1} were added. Additionally, fixed viscosity PVP solutions (~2.2 mPa·s) comprising 1 mol L^{-1}, 0.42 mol L^{-1}, and 0.07 mol L^{-1} PVP K-15, K-30, and K-90, respectively, were prepared. The gold target was then irradiated with a pulsed laser at room temperature for 60 minutes while stirring at 200 rpm. The resulting Au NP was used for further analyses. The microchip laser parameters were set as follows: wavelength of 1064 nm, pulse energy of 1.8 mJ, pulse duration of 900 ps, peak power of >2 MW, and a repetition rate of 100 Hz with an average power of 180 mW. The same parameter settings were used for all experiments.

Investigation of bubble formation and ablation mechanism using a high-speed camera.

The high-speed camera (HPV-2, Shimadzu Corporation, 312 × 260 pixels, maximum frame rate = 1000 kfps) was synchronized with the MCL using a function generator (Wave Factory, WF1943). One hundred images were recorded for MCL ablation at different frame

intervals: 4 ms for the solution viscosity experiment and 2 μs for investigating the PLAL mechanism with MCL. The gold sample was observed through an objective lens (Olympus, 2x, NA, 0.06) in front of the camera. An LED light source (THORLABS, DC20) was used for illumination. The liquid level was maintained at 5 mm above the gold surface, and the laser beam was focused directly on the target surface. The average spot diameter at the laser focus (130 ± 6 μm) was measured by ablating black ink on a glass substrate in the air, corresponding to a nominal laser fluence of 13.7 J cm^{-2} (pulse energy: 1.3 mJ/pulse). In the comparative experiment, the Nd:YAG laser was operated with Quanta-Ray PRO-250 (wavelength: 1064 nm; pulse energy: 1500 mJ; pulse duration: 12 ns; peak power: 125 MW; average laser power: 15 W; repetition rate: 10 Hz). For the experiment, the laser parameters were set as follows: wavelength: 1064 nm; pulse energy: 25 mJ; pulse duration: 12 ns; repetition rate: 10 Hz.

1-5. References

1. D. Zhang, Z. Li, K. Sugioka, *J. Phys. Photonics*, **2021**, *3*, 042002.
2. D. Zhang, B. Gökce, S. Barcikowski, *Chem. Rev.*, **2017**, *117*, 3990-4103.
3. H. Sakai, H. Kan, T. Taira, *Opt. Express*, **2008**, *16*, 19891-19899.
4. H. H. Lim, T. Taira, *Opt. Express*, **2022**, *30*, 5151-5158.
5. S. Dittrich, M. Spellauge, S. Barcikowski, H. P. Huber, B. Gokce, *Opto-Electron Adv.*, **2022**, *5*, 210053.
6. S. Dittrich, R. Streubel, C. McDonnell, H. P. Huber, S. Barcikowski, B. Gokce, *Appl. Phys. A*, **2019**, *125*, 432.
7. S. Dittrich, S. Barcikowski, B. Gokce, *Opto-Electron Adv.*, **2021**, *4*, 200072.
8. G. Raciukaitis, M. Brikas, P. Gecys, M. Gedvilas, *Proc. SPIE - The International Society for Optical Engineering*, **2008**, 7005.
9. R. Streubel, S. Barcikowski, B. Gokce, *Opt Lett.*, **2016**, *41*, 1486-1489.
10. J. Liu, W. Ong, E. Román, M. J. Lynn, A. E. Kaifer, *Langmuir*, **2000**, *16*, 3000-3002.
11. M. M. Alvarez, J. T. Khoury, T. G. Schaaff, M. N. Shafigullin, I. Vezmar, R. L. Whetten, *J. Phys. Chem. B*, **1997**, *101*, 3706.
12. F. Mafuné, J. Kohno, Y. Takeda, T. Kondow, H. Sawabe, *J. Phys. Chem. B*, **2001**, *105*, 5114-5120.
13. F. Mafuné, J. Kohno, Y. Takeda, T. Kondow, *J. Phys. Chem. B*, **2003**, *107*, 12589-12596.
14. H. Tsunoyama, H. Sakurai, N. Ichikuni, Y. Negishi, T. Tsukuda, *Langmuir*, **2004**, *20*, 11293-11296.
15. M. Okumura, Y. Kitagawa, T. Kawakami, M. Haruta, *Chem. Phys. Lett.*, **2008**, *459*, 133-136.
16. H. Tsunoyama, N. Ichikuni, H. Sakurai, T. Tsukuda, *J. Am. Chem. Soc.*, **2009**, *131*, 7086-7093.
17. J. Li, K. Inukai, Y. Takahashi, A. Tsuruta, W. Shin, *J. Asian Ceram. Soc.*, **2017**, *5*, 216-225.
18. S. Haesuwannakij, T. Kimura, Y. Furutani, K. Okumura, K. Kokubo, T. Sakata, H. Yasuda, Y. Yakiyama, H. Sakurai, *Sci. Rep.*, **2017**, *7*, 9579.
19. A. V. Kabashin, M. Meunier, C. Kingston, J. H. T. Luong, *J. Phys. Chem. B*, **2003**, *107*, 4527-4531.
20. T. Tsuji, D.-H. Thang, Y. Okazaki, M. Nakanishi, Y. Tsuboi, M. Tsuji, *Appl. Surf. Sci.*, **2008**, *254*, 5224-5230.

21. M.-R. Kalus, N. Bärsch, R. Streubel, E. Gökce, S. Barcikowski, B. Gökce, *Phys. Chem. Chem. Phys*., **2017**, *19*, 7112-7123.
22. S. Reich, P. Schönfeld, A. Letzel, S. Kohsakowski, M. Olbinado, B. Gökce, S. Barcikowski, A. Plech, *ChemPhysChem*, **2017**, *18*, 1084-1090.
23. T. Hupfeld, G. Laurens, S. Merabia, S. Barcikowski, B. Gökce, D. Amans, *J. Appl. Phys*., **2020**, *127*, 044306.
24. M.-R. Kalus, R. Lanyumba, S. Barcikowski, B. Gökce, *J. Flow Chem*., **2021**, *11*, 773-792.
25. M. Spellauge, C. Donate-Buendía, S. Barcikowski, B. Gokce, H. P. Huber, *Light. Sci. Appl*., **2022**, *11*, 68.
26. L. V. Zhigilei, Z. Lin, D. S. Ivanov, *J. Phys. Chem. C*, **2009**, *113*, 11892-11906.
27. M. Senegacnik, K. Kunimoto, S. Yamaguchi, K. Kimura, T. Sakka, P. Gregorcic, *Ultrason. Sonochem.*, **2021**, *73*, 105460.
28. A. Letzel, S. Reich, T. dos Santos Rolo, A. Kanitz, J. Hoppius, A. Rack, M. P. Olbinado, A. Ostendorf, B. Gokce, A. Plech, S. Barcikowski, *Langmuir*, **2019**, *35*, 3038-3047.
29. K. Mehta, S. Soumyashree, J. Pandya, P. Singh, R. K. Kushawaha, P. Kumar, S. Shinde, J. Saha, P. K. Baruah, *Appl. Phys. A*, **2023**, *129*, 388.
30. K. Oguchi, M. Enoki, N. Hirata, *Mater. Trans.*, **2015**, *56*, 534-538.
31. A. Vogel, S. Busch, U. Parlitz, *J. Acoust. Soc. Am*., **1996**, *100*, 148.
32. W. Soliman, N. Takeda, K. Sasaki, *Appl. Phys. Expr*. **2010**, *3*, 35201
33. F. Mafuné, J. Kohno, Y. Takeda, T. Kondow, *J. Phys. Chem. B*, **2001**, *105*, 9050-9056.
34. J. Crank, The mathematics of diffusion, Oxford Univ. Press, London, **1957**, 11.
35. L. Costigliola, D. M. Heyes, T. B. Schrøder, J. C. Dyre, *J. Chem. Phys*., **2019**, *150*, 021101.

Chapter 2

Mechanistic Study in Gold Nanoparticle Synthesis through Microchip Laser Ablation in Organic Solvents

2-1. Introduction

Gold nanoparticles (Au NPs) are notable for their strong absorption of visible electromagnetic waves through surface plasmon resonance. This characteristic, along with their ability to remain evenly dispersed in a matrix, makes Au NPs valuable in various fields, including sensors, electronics, medical treatments, solar cells, drug delivery, and catalysis [1,2]. While Au NPs can be synthesized in both hydrophilic and hydrophobic media, achieving the desired NPs in organic solvents requires more complex and meticulous steps due to the low solubility of gold salts in organic phases. Proper dispersion and stabilization of gold salts within non-aqueous liquid phases are crucial [3-6]. Pulsed laser ablation in liquids (PLAL) has recently gained interest as a method for generating metal NPs due to its advantages, such as the absence of reducing agents, operational simplicity, high purity without purification steps, and suitability for biological and medical applications [7,8].

PLAL can utilize various organic solvents such as DMSO, DMF, MeCN, THF, acetone, alkanes, and aromatic compounds like toluene. The choice of solvent influences the results based on its physical properties, with organic solvents often leading to the formation of carbon-coated NPs [9,10], which maintain small particle sizes and allow further functionalization. Amendola et al. demonstrated that NP size and aggregation could be controlled by adjusting laser parameters in solvents like DMSO, MeCN, and THF [11]. Giorgetti et al. found that Au NPs ablated in acetone showed enhanced stability and fluorescent properties compared to those in water [12]. Compagnini et al. showed surface functionalization with alkanethiols during ablation in alkane/alkane-thiol solutions [13]. Additionally, the physical properties of the chosen solvent, such as density [14], viscosity [15], polarity [16], and thermal reactivity [17], impact the outcome of the pulsed laser ablation process. High-power laser systems face limitations when applied to low boiling point organic solvents due to flammability concerns. This limitation is addressed by employing the MCL system for PLAL.

The MCL's short cavity length of less than 10 mm makes it portable and suitable for standard organic synthesis laboratories. It directly applies generated metal NPs to catalytic reactions via in situ operations. The MCL's pulse duration of 0.9 ns minimizes pulse energy losses due to the shielding effect of the ablation plume and cavitation bubble, which occur between 1 and 5 ns after the pulse. A key advantage is the reduced laser power (average power

of 50 mW), allowing the use of many low boiling point organic solvents in PLAL. Additionally, the MCL's low repetition rate (100 Hz) prevents heat accumulation, enabling the use of various organic solvents without concerns about flammability.

In the prior chapter, Au NPs were successfully generated in aqueous poly(*N*-vinyl-2-pyrrolidone) (PVP) solutions using the MCL system [18]. Building on this, this chapter presents a study on the preparation of Au NPs in various organic solvents (CH_2Cl_2, $CHCl_3$, 2-PrOH, MeCN, DMF, EtOH, NMP, and DMSO), with PVP as a stabilizing agent. Due to low pulse energy and the thermal conductivity of the solvents, multiple laser pulses were necessary for successful Au NP production, a phenomenon known as the 'incubation effect.' This highlights the need to consider experimental parameters and solvent characteristics for precise NP synthesis.

2-2. Results and Discussion

The inclusion of other materials in the organic solvent affects the ablation event. For instance, PVP is commonly used as a stabilizing agent for metal colloids in chemical reduction methods [19,20], and its concentration and chain length significantly influence the resulting particle size and catalytic reaction efficiency. PVP has also been employed in PLAL [21,22], affecting the final particle size of silver NPs due to solubility differences in various solvents [23]. However, existing literature lacks research on the influence of non-aqueous PVP solution on Au NP particle size and ablation efficiency during laser ablation in organic solvents. To address this gap, the investigation focused on how particle size and ablation efficiency change depending on the reaction solvent. Notably, PVP (K-15) was used at a concentration of 0.1 M in this study, as previous research confirmed that both the molecular weight and concentration of PVP do not impact the size of generated Au NPs [18].

Table 1. PLAL on gold target in organic solvents with PVP (K-15).

Solvent	Particle size (nm)	Au productivity (μg/h)	Viscosity (mPa·s)	Thermal conductivity (W/m·K)	Required number of pulse
CH_2Cl_2	3.2 ± 0.7	79.3	0.68 ± 0.02	0.13	1
$CHCl_3$	3.5 ± 1.0	109.1	0.67 ± 0.02	0.12	1
2-PrOH	4.4 ± 1.1	134.7	2.92 ± 0.02	0.16	3
MeCN	3.5 ± 0.7	147.5	0.45 ± 0.02	0.15	4
DMF	3.4 ± 0.8	155.2	1.12 ± 0.02	0.16	4
EtOH	3.4 ± 0.8	166.8	1.81 ± 0.02	0.17	6
NMP	3.3 ± 0.4	168.6	2.16 ± 0.02	0.18	6
DMSO	3.0 ± 0.8	173.1	2.72 ± 0.02	0.20	6

This study investigated the impact of various solvents on particle size and Au productivity in the presence of PVP K-15 using PLAL with the MCL system (1.8 mJ/pulse, 100 Hz). Eight organic solvents were tested: dichloromethane (CH_2Cl_2), chloroform ($CHCl_3$), isopropanol (2-PrOH), acetonitrile (MeCN), dimethylformamide (DMF), ethanol (EtOH), *N*-methyl-2-pyrrolidone (NMP), and dimethyl sulfoxide (DMSO). Au NPs were successfully produced in all solvents, with particle sizes confirmed by TEM measurements (Table 1), consistently ranging from 3 to 4 nm. This consistency aligns with results from aqueous PVP solutions [18]. The MCL system's characteristics of low pulse energy and repetition rate result in small, short-lived cavitation bubbles, limiting NP nucleation and growth. PVP, being soluble in all solvents, does not affect NP size due to solubility issues but effectively quenches NP growth after bubble collapse. Ablation efficiency varied with solvent type, particularly between halogenated solvents (CH_2Cl_2 and $CHCl_3$) and others (Table 1). Factors influencing PLAL ablation efficiency include solution viscosity, as tiny gas bubbles in viscous media absorb, reflect, and scatter laser energy, lowering ablation efficiency [18].

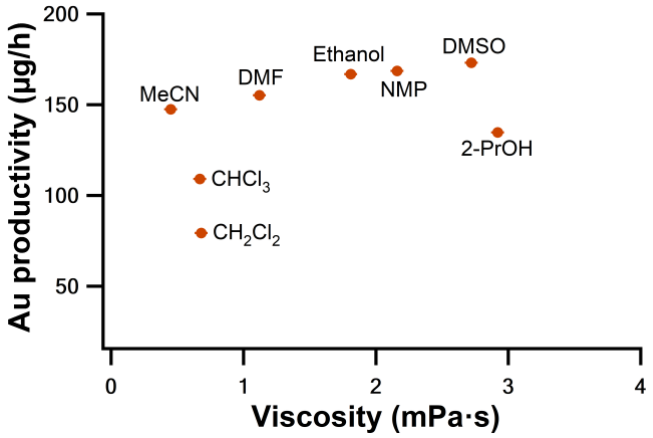

Figure 1. Viscosity effect on Au NPs productivity.

In this study, the correlation between the yield of Au NPs and the viscosity of organic solvents in the presence of PVP was initially examined. However, no clear relationship was observed (Table 1, Figure 1). This suggests that the yield of Au NPs is influenced more by the type of organic solvent than by the system viscosity when PVP is present. Consequently, other factors that might affect gas bubble formation, such as the activation energy for solvent pyrolysis and vaporization enthalpy, were explored. It has been reported that gas bubble formation is linearly related to the activation energy of solvent pyrolysis [24]. This pyrolysis occurs at high temperatures and pressures, producing carbon products like a carbon shell. However, in the analysis, no carbon shell formation was observed on the surface of Au NPs, likely due to the low laser power of the MCL system. Therefore, the activation energy for pyrolysis was assumed not to significantly affect ablation efficiency.

Solvents with low vaporization enthalpy decompose more easily, forming gas bubbles that reduce laser ablation efficiency [24]. In this experiment, CH_2Cl_2 and $CHCl_3$, having lower

vaporization enthalpies (CH_2Cl_2: 28.5 kJ/mol, $CHCl_3$: 30.5 kJ/mol) compared to other solvents (2-PrOH: 46.0 kJ/mol, MeCN: 33.8 kJ/mol, DMF: 46.7 kJ/mol, Ethanol: 42.3 kJ/mol, NMP: 55.3 kJ/mol, DMSO: 52.9 kJ/mol) [25], likely produced more gas bubbles, resulting in reduced ablation efficiency. Additionally, experiments without PVP showed a significant yield decrease in CH_2Cl_2 and $CHCl_3$ (40-70 µg/h), while other solvents had minor deviations (9-14 µg/h) (Figure 2a). PVP reportedly increases the system's heat capacity, thereby reducing gas bubble formation [26]. These findings suggest that PVP's effect is more significant in solvents with low vaporization enthalpy, whereas it is less impactful in solvents with higher vaporization enthalpy.

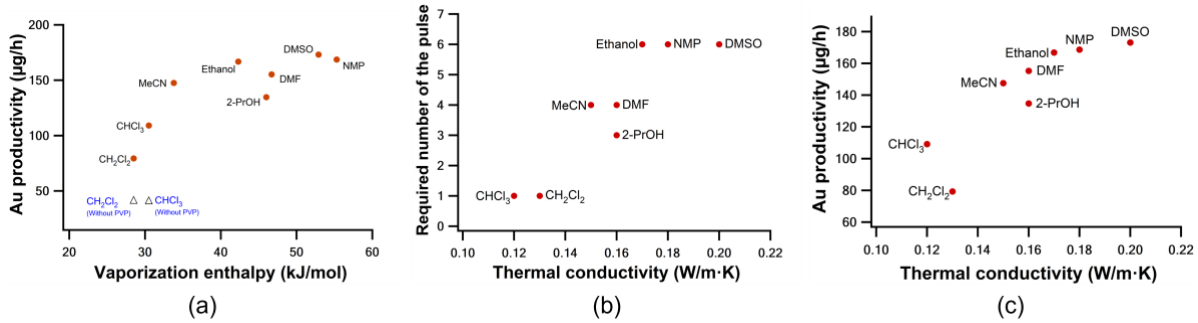

Figure 2. (a) Plot of the ablated Au amount versus vaporization enthalpy (Red circles represent all of the solvents in the presence of PVP, and black triangle represents the CH_2Cl_2 and $CHCl_3$ in the absence of PVP), (b) the required number of the pulse versus thermal conductivity in the presence of PVP, and (c) ablated Au amount versus vaporization enthalpy in the presence of PVP.

Real-time monitoring of the ablation in organic media

To gain insight into the underlying mechanism behind ablation efficiency in MCL-based PLAL using organic solvents in the presence of PVP K-15, the ablation process of Au NPs was monitored in real-time with a high-speed camera, capturing images at 250 µs per frame during initial laser ablation. Figure 3 shows the generation of Au NPs at different laser pulses in various organic solvents, contrasting the typical laser ablation where a single pulse can ablate the metal target [27-28]. High energy localization at the target surface is necessary for ablation, but this is often suppressed by laser beam reflection and heat diffusion into the target [29]. In this case, low induced energy did not reach the ablation threshold due to low pulse energy, associated with the incubation behavior of the ablation threshold fluence, where the threshold decreases with an increasing number of pulses, forming a rougher target surface (Figure 4) [29]. This phenomenon has been investigated under various conditions, including vacuum [30,31], aqueous environments [32,33], and recent computational studies [34]. Byskov-Nielsen reported that incubation effects are more significant in the low-fluence regime,

while at high fluence, plasma is generated due to sufficient energy for the ablation threshold [29]. In the experiments, a pulse energy of 1.8 mJ (13.5 J/cm²) was used, contributing to the observed incubation effect. Another factor may be heat diffusion from the bulk gold surface to the surrounding solvent. Differences in heat dissipation from the gold surface to the solvent, determined by the solvent's thermal conductivity, affect the superheated degree of the molten surface. Figure 2 and Table 1 confirm a linear correlation between the thermal conductivity of organic solvents and both the incubation effect and ablation efficiency [35,36].

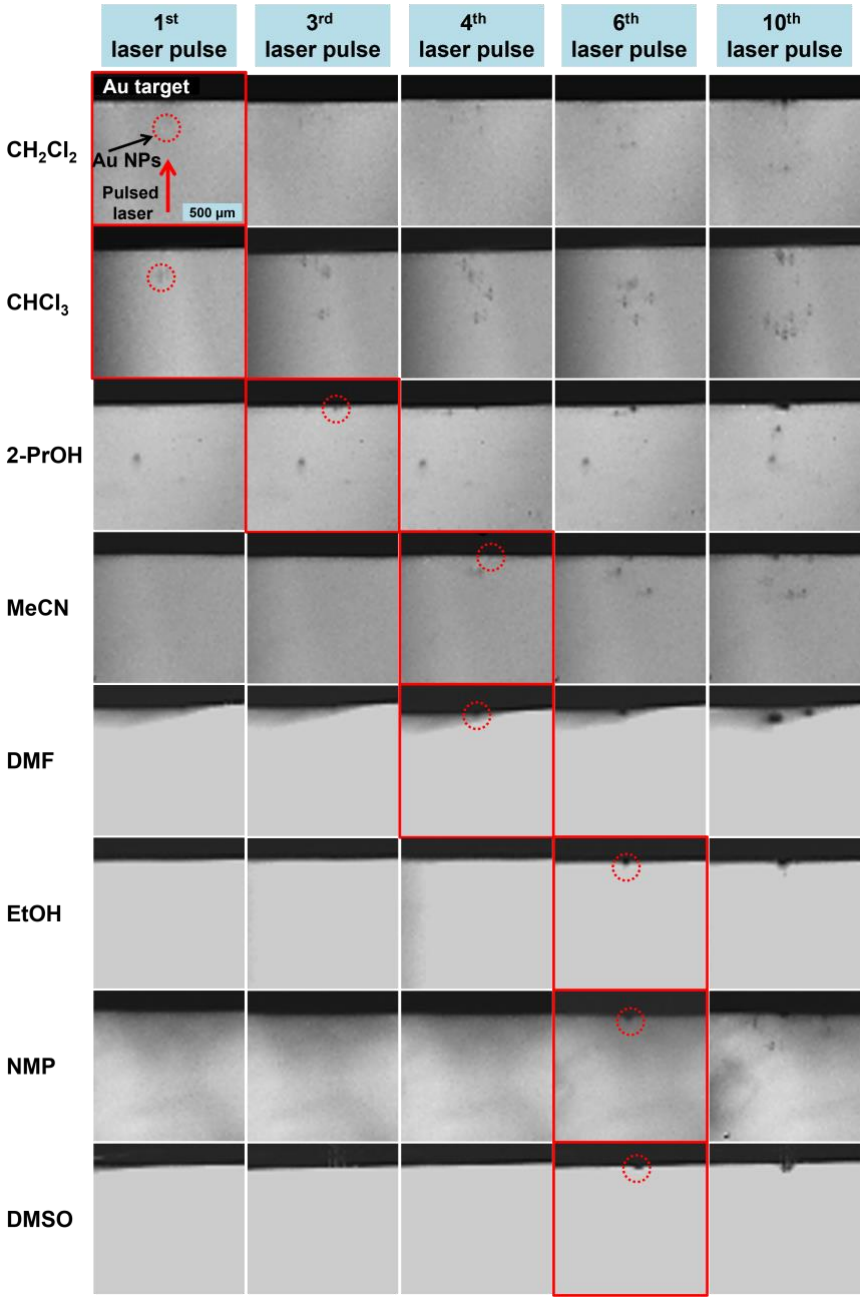

Figure 3. Selected videographic images of Au NP ablation in different organic solvents in the presence of PVP K-15 (0.1 M) by MCL. Au NP generation in each solvent started after different numbers of laser pulses (highlighted by a red square). In each solvent, the ejected Au NPs from the corresponding laser pulse were indicated by a red circle. Pulsed laser, marked by a red arrow, which was irradiated vertically from top to bottom. However, the resulting image captured by the camera was inverted, showing the opposite direction. In the 2-PrOH sample, previously generated metal NPs are present as contamination due to several attempts to position and achieve precise imaging for accurate ablation.

In this context, CH_2Cl_2 and $CHCl_3$ have lower thermal conductivity compared to other solvents, meaning they do not dissipate heat effectively from the gold target surface (Figure 4a) [37].

Consequently, a single laser pulse may suffice to vaporize and ablate the bulk gold target without any incubation effect. On the other hand, ethanol, NMP, and DMSO solvents have higher thermal conductivity, enabling more effective heat dissipation from the gold target surface (Figure 4b) [37]. Thus, the ablation threshold and energy localization are not achieved, necessitating multiple laser pulses. The ablation efficiency increases with the number of laser shots, as shown in Table 1 (Au productivity from ICP-AES analysis). This is due to the increased roughness of the bulk gold surface. Under irradiation, a superheated layer on the target surface stabilizes through rapid cooling and resolidifying, creating surface roughness [33]. This roughness enhances energy localization due to significantly lower heat diffusion lengths, reducing heat diffusivity. As a result, heat dissipation is minimized, lowering the ablation threshold and improving material ablation efficiency (Figure 4).

The experimental results showed that thermal conductivity determines the number of laser pulses needed for Au NP ablation and influences the target surface roughness. Vaporization enthalpy affects gas bubble formation during ablation, but this shielding effect is less noticeable in solvents with high vaporization energy (>33 kJ/mol, such as MeCN). These findings suggest that solvent thermal conductivity is the primary factor affecting ablation efficiency, with vaporization enthalpy as a secondary factor, particularly in low-vaporization solvents without polymers.

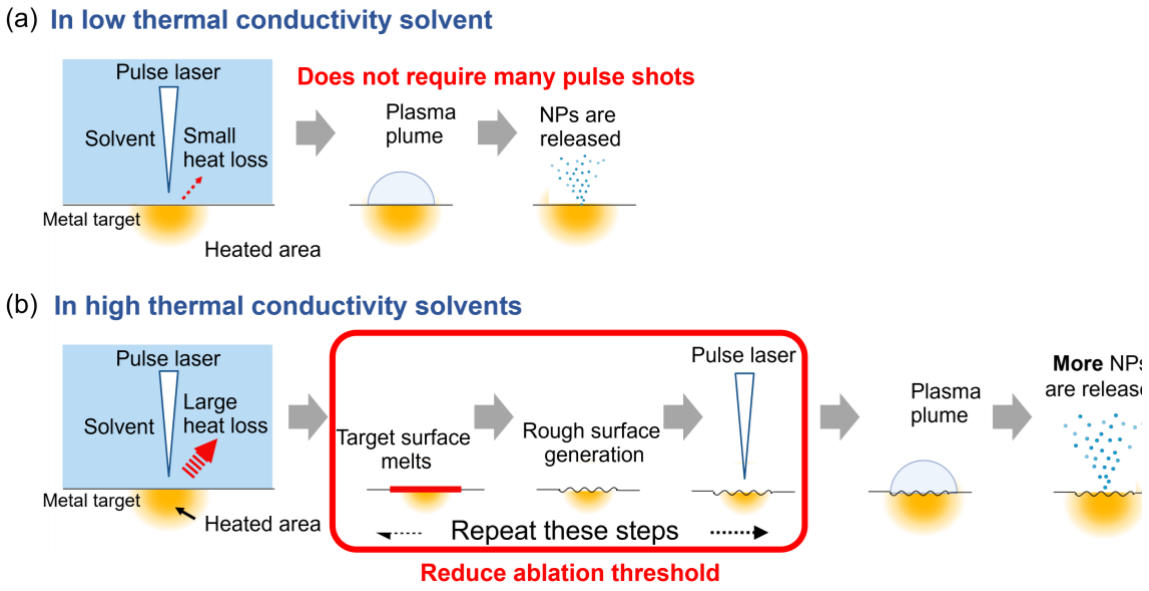

Figure 4. Schematic representation of laser ablation mechanism in (a) low thermal conductivity solvents and (b) high thermal conductivity solvents.

2-3. Conclusions

This study demonstrated the preparation of Au NPs in various organic solvents using PLAL with an MCL system. The research consistently produced small Au NPs with PVP present across different solvents. It examined the influence of different organic solvents on the ablation efficiency of Au NPs, revealing that the solvent choice significantly impacted the number of laser pulses needed for NP generation. This effect was linked to the incubation effect and correlated with the laser energy applied and the solvent's thermal conductivity. Solvents with higher thermal conductivity showed improved ablation efficiency. Additionally, vaporization enthalpy emerged as a significant factor, particularly in solvents with low vaporization enthalpy and without polymers. This innovative method addresses the challenges of using high-power laser systems with flammable solvents, presenting a promising approach for advanced NP synthesis. The findings offer valuable insights into the factors affecting PLAL in non-aqueous media and guide the optimization of NP production in various solvent environments.

2-4. Experimental Section

Materials

Commercially purchased reagents were used without further purification unless specified. Ultrapure water (18.2 $\Omega \cdot cm^{-1}$) was prepared using an Organo Puric-ω system. Transmission Electron Microscopy (TEM) images were captured with a JEM-2100 electron microscope (JEOL, Tokyo, Japan) at 200 kV. A holey carbon support film-coated Cu microgrid U1003 (EM Japan, Tokyo, Japan) was used, with hydrophilic treatment via glow discharge irradiation. Image-J software (version 1.52a) analyzed TEM images with mean diameter and standard deviation values from measurements of 300 particles. Inductively Coupled Plasma Atomic Emission Spectroscopy (ICP-AES) was performed using an ICPS-8100 (Shimadzu, Kyoto, Japan). Viscosity measurements utilized the HAAKE RheoStress 6000 (Thermo Scientific, Waltham, MA, USA) at a shear rate of 1000 s^{-1} and 25 °C. No significant viscosity differences were observed between pre-and post-PLAL conditions, so all viscosity measurements were taken post-PLAL.

General PLAL method

A gold target (>99.99%, 5 × 15 mm) was ultrasonically cleaned in acetone for 5 minutes and rinsed with deionized water. The target was then mounted on a custom-made PEEK holder with a magnetic stir bar and placed at the bottom of a Pyrex® vessel (30 × 80 mm). Zirconia beads (φ 6 mm) were used to stabilize the holder's rotation. Into this vessel, 15 mL of 0.1 M poly(*N*-vinyl-2-pyrrolidone) (PVP) (K-15 (10 kDa))/organic solvent (CH_2Cl_2, $CHCl_3$, 2-PrOH, MeCN, DMF, EtOH, NMP, and DMSO) was added. The gold target was exposed to pulsed laser irradiation at room temperature for 60 minutes while rotating at 200 rpm. A parallel experiment without PVP in each organic solvent was also conducted. The laser parameters were: wavelength 1064 nm, pulse energy 1.8 mJ, pulse duration 900 ps, average power 180 mW, and repetition rate 100 Hz. The resulting Au NPs were then analyzed. Pulse energy adjustments were made by varying the applied current.

Real-time monitoring using a high-speed camera

A high-speed camera (HPV-2, Shimadzu Corporation, 312 × 260 pixels, maximum frame rate = 1000 kfps) was synchronized with the MCL using a function generator WF1943 (Wave Factory, Yokohama, Japan). For MCL ablation, 100 images were recorded with 250 μs frame intervals for organic solutions (CH_2Cl_2, $CHCl_3$, 2-PrOH, MeCN, DMF, EtOH, NMP, and DMSO) containing PVP K-15 at 0.1 M concentration. A parallel experiment was

conducted without PVP. The gold sample was observed through a 2× objective lens, NA 0.06 (Olympus, Tokyo, Japan), positioned in front of the camera. An LED light source DC20 (THORLABS, Newton, NJ, USA) provided illumination. The liquid level was maintained at 5 mm above the gold surface, and the laser beam was focused directly on the target surface. The average spot size at the laser focus was 130 ± 6 μm, measured by ablating black ink on a glass substrate in air, corresponding to a nominal laser fluence of 13.5 J/cm² (several times higher than the ablation threshold fluence of 2.1 J/cm²).

2-5. References

1. N. Li, P. Zhao, D. Astruc, *Angew. Chem. Int. Ed*., **2014**, *53*, 1756-1789.
2. J. Zhang, L. Mou, X. Jiang, *Chem. Sci*., **2020**, *11*, 923-936.
3. N. A. Sapoletova, S. E. Kushnir, A. E. Kushnir, P. B. Kocherginskaya, P. E. Kazin, K. S. Napolskii, *RSC Adv*., **2016**, *6*, 112409-112412.
4. V. V. Terekhin, I. N. Senchikhin, O. V. Dement'eva, V. M. Rudoy, *Colloid Journal*, **2015**, *77*, 511-519.
5. T. Sachin, C. N. Trupti, M. Shaebrao, D. A. Jalindar, B. K. Bharat, D. K. Nageshawar, *Langmuir*, **2019**, *35*, 9213-9218.
6. M. Cao, Q. Liu, M. Chen, P. Yang, Y. Xu, H. Wu, J. Yu, L. He, X.-H. Zhang, Q. Zhang, *RSC Adv*., **2017**, *7*, 25535-25541.
7. D. Zhang, Z. Li, K. Sugioka, *J. Phys. Photonics*, **2021**, **3**, 042002.
8. D. Zhang, B. Gökce, S. Barcikowski, *Chem. Rev*., **2017**, *5*, 3990-4103.
9. V. Amendola, S. Polizzi, M. Meneghetti, *Langmuir*, **2007**, *23*, 6766-6770.
10. D. Zhang, C. Zhang, J. Liu, Q. Cen, X. Zhu, C. Liang, *ACS Appl. Nano Mater.*, **2019**, *2*, 28-39.
11. V. Amendola, S. Polizzi, M. Meneghetti, V. Amendola, *J. Phys. Chem. B*, **2006**, *110*, 7232-7237.
12. E. Giorgetti, M. Muniz-Miranda, P. Marsili, D. Scarpellini, F. Giammanco, *J. Nanopart. Res.*, **2012**, *14*, 648.
13. G. Compagnini, A. A. Scalisi, O. Puglisi, C. Spinella, *J. Mater. Res.*, **2004**, *19*, 2795-2798.
14. J. Long, M. H. Eliceiri, L. Wang, Z. Vangelatos, Y. Ouyang, X. Xie, Y. Zhang C. P. Grigoropoulos, *Opt. Laser Technol*., **2021**, *134*, 106647.
15. M.-R. Kalus, R. Lanyumba, S. Barcikowski, B. Gokce, *J. Flow Chem*., **2021**, *11*, 773-792.
16. G. Forte, L. D'Urso, E. Fazio, S. Patane, F. Neri, O. Puglisi, G. Compagnini, *Applied Surface Science*, **2013**, *272*, 76-81.
17. R. Rawat, A. Tiwari, N. Arun, S. V. S. N. Rao, A.P. Pathak, Y. Shadangi, N. K. Mukhopadhyay, S. V. Rao, A. Tripathi, *Journal of Alloys and Compounds*, **2021**, *859*, 157871.
18. B.S. Hettiarachchi, Y. Takaoka, Y. Uetake, Y. Yakiyama, H. H. Lim, T. Taira, M. Maruyama, Y. Mori, H. Y. Yoshikawa, H. Sakurai, *Ind. Chem. Mater.*, **2024**. *2*, 340-347.

19. R. N. Dhital, K. Nomura, Y. Sato, S. Haesuwannakij, M. Ehara, H. Sakurai, *Bull. Chem. Soc. Jpn.*, **2020**, *93*, 1180-1185.
20. Y. Uetake, S. Mouri, S. Haesuwannakij, K. Okumura, H. Sakurai, *Nanoscale Adv.*, **2021**, *3*, 1496-1501.
21. T. Tsuji, D.-H Thang, Y. Okazaki, M. Nakanishi, Y. Tsuboi, M. Tsuji, *Appl. Surf. Sci.*, **2008**, *254*, 5224-5230.
22. A. Letzel, S. Reich, T. dos Santos Rolo, A. Kanitz, J. Hoppius, A. Rack, M. P. Olbinado, A. Ostendorf, B. Gökce, A. Plech, A.; *Langmuir*, **2019**, *35*, 3038-3047.
23. S. Kassavetis, S. Kaziannis, N. Pliatsikas, A. Avgeropoulos, A. E. Karantzalis, C. Kosmidis, E. Lidorikis, P. Patsalas, *Appl. Surf. Sci*., **2015**, *336*, 262-266.
24. T. Fromme, L. K. Tintrop, S. Reichenberger, T. C. Schmidt, S. Barcikowski, *ChemPhysChem*., **2023**, *24*, e202300089.
25. J. S. Chickos, Heat of Sublimation Data. In *NIST Chemistry WebBook*; NIST Standard Reference Database Number 69; P. J. Linstrom, W. G. Mallard, Eds.; National Institute of Standards and Technology: Gaithersburg, MD, USA, **2020**; p. 20899.
26. L. H. Sperling, Introduction to Physical Polymer Science, Wiley-Inter Science, New York, **1992**, p.87
27. M. Spellauge, C. Doñate.-B, S. Barcikowski, B. Gökce, H. P. Huber, *Light Sci. Appl*., **2022**, *11*, 68.
28. M. Senegačnik, K. Kunimoto, S. Yamaguchi, K. Kimura, T. Sakka, P. Gregorčič, *Ultrasonics Sonochemistry*, **2021**, *73*, 105460.
29. J. Byskov-Nielsen, J. M. Savolainen, M. S. Christensen, P. Balling, *Appl. Phys. A*, **2010**, *101*, 97-101.
30. S. E. Kirkwood, A. C. van Popta, Y. Y. Tsui, R. Fedosejevs, *Appl. Phys. A: Mater. Sci. Process*., **2005**, *81*, 729-735.
31. J. Krüger, D. Dufft, R. Koter, A. Hertwig, *Appl. Surf. Sci*., **2007**, *253*, 7815-7819.
32. M.-R. Kalus, S. Barcikowski, B. Gökce, *Chem. Eur. J*., **2021**, *27*, 5978.
33. S. Reich, A. Letzel, B. Gökce, A. Menzel, S. Barcikowski, A. Plech, *ChemPhysChem*., **2019**, *20*, 1036.
34. C.-Y. Shih, M. V. Shugaev, C. Wu, L. V. Zhigilei, *J. Phys. Chem. C*., **2017**, *121*, 16549-16567.
35. Q.-F. Lei, R.-S. Lin, D.-Y. Ni, Y.-C. Hou, *J. Chem. Eng. Data*., **1997**, *42*, 971-974.
36. T. E. Daubert, R. P. Danner, Physical and Thermodynamic Properties of Pure Chemicals: Data Compilation, Taylor & Francis, Washington, DC, **1989**.

37. P. Ouyang, P. Li, E. G. Leksina, S. V. Michurin, L. He, *Appl. Surf. Sci*., **2016**, *360*, 880-888.

Chapter 3

Tailoring Carbon-Encapsulated Gold Nanoclusters via Microchip Laser Ablation in Polystyrene Solution: Controlling Size, Structure, and Photoluminescent Properties

3-1. Introduction

Carbon-encapsulated metal nanoparticles (NPs) have gained significant attention due to their diverse applications, including catalysis and biomedical engineering [1,2]. These nanostructures exhibit remarkable properties, particularly their superior catalytic activity in Fenton-like reactions [3]. Moreover, incorporating heteroatom dopants, such as metal NPs encapsulated within N, P-doped carbon [4], along with the favorable metal-carbon interface, has been found to promote efficient electron transfer, further improving catalytic performance [5]. Typically, the synthesis of carbon-encapsulated metal NPs involves reducing metal ions, followed by their encapsulation within a carbon shell [6]. Several techniques are available for coating the NP surface, including vapor deposition [7], sol-gel [8], and solution dipping [9].

Pulsed laser ablation in liquid (PLAL) presents a highly efficient single-step approach for producing these nanostructured materials under ambient conditions [10-12]. During PLAL, intense laser pulses strike a metal target, generating a plasma plume where metal NPs are formed. Under extreme temperature and pressure conditions within the plasma, solvent molecules break down, producing carbon species. These carbon fragments subsequently condense onto the metal surface, leading to the formation of an encapsulated structure [10,13-15]. Among the solvents frequently employed in PLAL, toluene and benzene serve as both solvents and carbon precursors for synthesizing carbon-encapsulated metal NPs. The thickness of the carbon shell is a critical factor influencing its functionality, particularly in surface-enhanced Raman scattering (SERS) applications [16]. In these cases, ultrathin carbon layers are preferred to maximize SERS efficiency and to fine-tune the surface plasmon characteristics of Au NPs. Additionally, reducing NP size increases the density of surface-active sites, significantly enhancing catalytic performance [17]. However, achieving ultra-small NPs with thin carbon coatings remains a challenge.

In Chapters 1 and 2, my investigations demonstrated that MCL effectively generates gold NPs in both aqueous and polar organic solvents, stabilized using poly(*N*-vinyl-2-pyrrolidone) (PVP), a hydrophilic polymer [18,19]. The MCL technique successfully overcomes the challenges posed by high-power laser systems when working with flammable organic solvents, making it a promising method for advanced NP synthesis. Building upon

these advantages, the study was extended to examine the synthesis of gold nanoclusters (Au NCs) with diameters below 2 nm, stabilized using polystyrene, a hydrophobic polymer, in toluene. The incorporation of polystyrene enabled precise control over particle size distribution and toluene decomposition due to its high heat capacity [20], ultimately yielding monodispersed small Au NCs with an ultrathin carbon shell. Additionally, the carbon layer produced via laser ablation exhibited visible-region luminescence with wavelength-dependent properties similar to typical carbon dots, further expanding the potential applications of these novel nanomaterials.

3-2. Results and Discussion

MCL ablation in polystyrene solution

The experiment commenced with the irradiation of a bulk gold target using a 180 mW laser in a 50 mM polystyrene-dissolved toluene solution for one hour. Throughout the ablation process, the solution's color changed from transparent to brown. As depicted in Figure 1(a-c), TEM analysis verified the formation of Au NCs, exhibiting a primary particle size of 1.7 ± 0.3 nm with a remarkably narrow size distribution. This particle size is consistent with findings in the literature, where carbon materials are generated via PLAL in toluene [10,14]. Typically, PLAL yields metal NPs exceeding 5 nm [21]. The observed particle characteristics suggest that

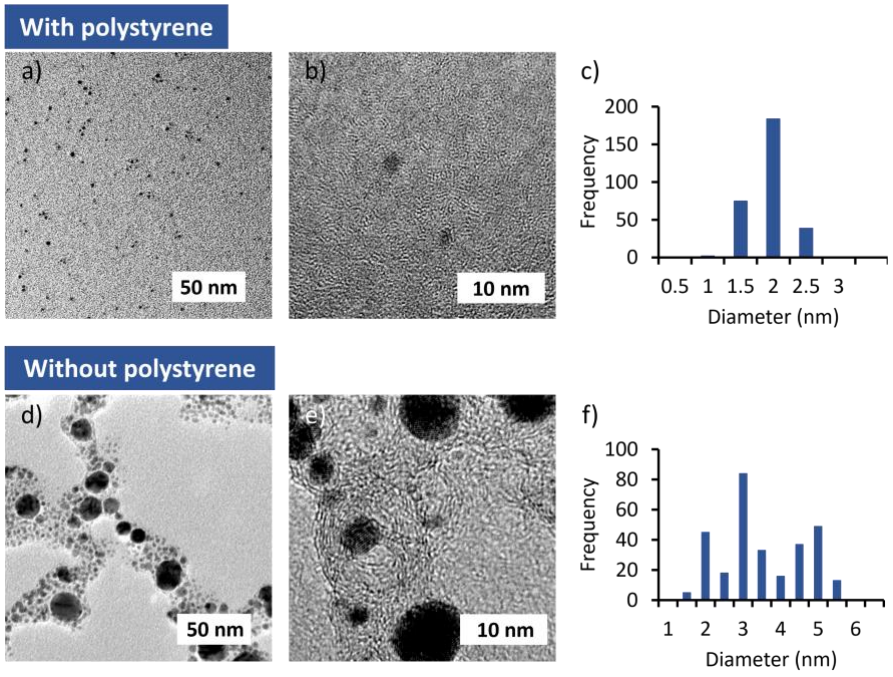

Figure 1 a), b), d), e) TEM images and c), f) size distribution of Au NCs prepared a)-c) under polystyrene and d)-f) in the absence of polystyrene. The applied average energy was 180 mW for each.

the encapsulation of Au NCs within a carbon matrix, resulting from solvent decomposition, significantly influences the process. This encapsulation effectively suppresses particle nucleation and growth, leading to smaller primary particle sizes.

Additionally, Au NCs were synthesized in toluene without polystyrene. As presented in Figure 1(d-f), the resulting Au NCs exhibited three distinct primary particle size fractions (1.8 nm 19%, 2.8 nm 44%, 4.5 nm 37%) surrounded by thicker graphitic carbon layers. This outcome differs from previous literature, which reports a uniform size distribution [10], possibly due to the higher laser fluence in this system (19.6 J/cm²). Based on previous studies on nanoparticle formation [15,22], potential mechanisms underlying the formation of varying carbon-encapsulated NC sizes are illustrated in Figure 2. When a pulsed laser irradiates the bulk gold target, Au particles undergo ablation under the extreme temperature and pressure conditions of the plasma plume. Recent studies indicate that particle growth initiates within the plasma plume during the initial nanoseconds of the process, ultimately yielding multiple-size distributions [23,24]. Under these conditions, toluene molecules rapidly decompose, generating carbon species that condense onto the ablated Au NCs, forming a carbon layer. In the absence of a stabilizing agent, the resulting nanostructures experience multiple aggregation stages due to Brownian motion and Van der Waals forces [25]. Conversely, in the presence of

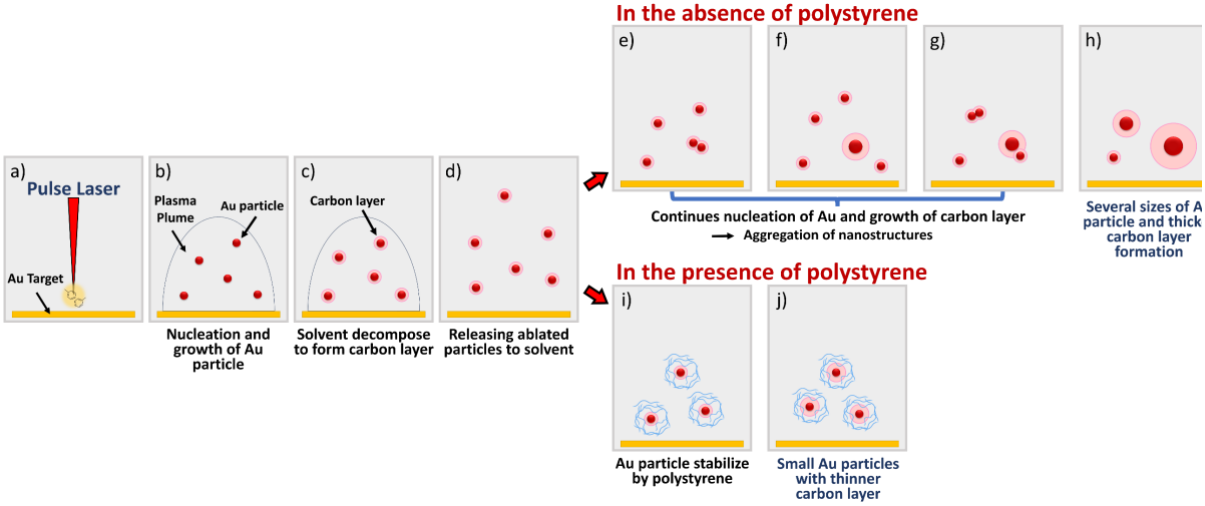

Figure 2. Schematic representation of the formation of carbon-encapsulated nanostructures. When a pulsed laser irradiates a bulk gold target (a), Au particles are ablated in the plasma plume (b). The decomposition of toluene generates carbon, which condenses onto the surface of the Au particles, forming carbon-encapsulated nanostructures (c). Then, these nanostructures are released to the surrounding solvent (d). In the absence of a stabilizing agent, these nanostructures tend to aggregate, leading to growth in particle size and an increase in the number of carbon layers (e)-(g). Thus, nanostructures with varying sizes are produced (h). In the presence of polystyrene, which adsorbs polystyrene onto the encapsulated nanostructures, further aggregation is prevented (i), (j).

polystyrene, adsorption onto the forming Au core or the carbon layer surrounding it restricts further core growth and prevents aggregation, leading to smaller and more uniform particles.

Regarding the carbon layer thickness (Figure 1(b) and Figure 3), it was observed that the sample containing polystyrene exhibited a comparatively thinner layer. This suggests that NC size influences carbon layer thickness due to cooling effects (carbon pyrolysis) [22] and the spatial distribution of decomposed carbon within the plasma plume (carbon segregation) [26]. The slightly larger clusters obtained in the absence of polystyrene indicate the contribution of these effects. Additionally, polystyrene's high heat capacity reduces the extent of toluene decomposition, leading to thinner carbon layers.

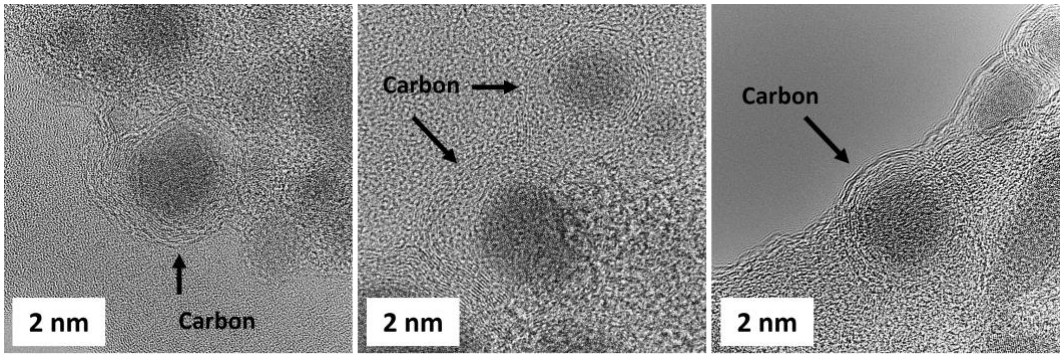

Figure 3. HRTEM image of carbon-encapsulated Au NCs prepared with 104 mW laser power in the presence of 400 mM polystyrene.

Beyond primary particle size analysis, secondary particle size was also assessed using dynamic light scattering (DLS) to highlight structural differences in PLAL products synthesized with and without polystyrene. As illustrated in Figure 4, samples containing polystyrene had an average secondary particle diameter of 7.3 nm, whereas those synthesized in pure toluene exhibited a significantly larger average diameter of 2.4 × 10^2 nm, corresponding to aggregated carbon structures as confirmed by TEM analysis.

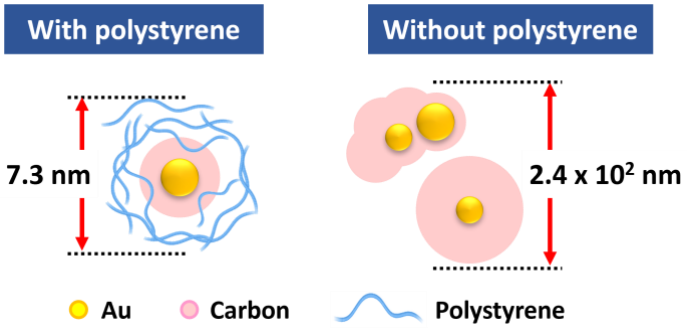

Figure 4. Schematic structural model and secondary particle size of carbon-encapsulated Au NCs in the presence and absence of polystyrene (after 15 minutes of sonication).

Raman spectral measurements provided further insights into the carbon layer's structure (Figure 5). Each sample displayed two broad peaks around 1350 cm^{-1} and 1570 cm^{-1},

corresponding to the D and G bands of carbon, respectively. The obtained carbon structures closely resembled those reported by Chieu et al., who synthesized carbon through benzene pyrolysis, as indicated by their similar Raman spectra [27].

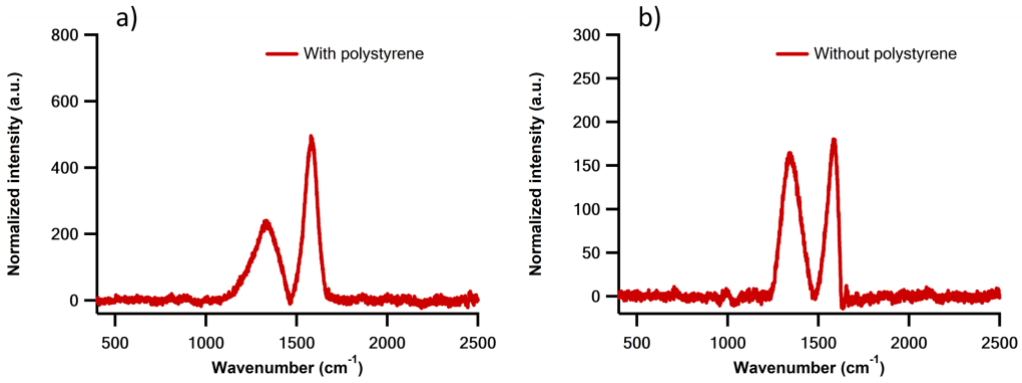

Figure 5. Raman spectrum of the carbon-encapsulated Au NCs (A) in the presence and (B) absence of polystyrene, respectively.

UV/Visible absorption spectra revealed comparable absorption properties in both prepared samples (Figure 6). A broad surface plasmon resonance (SPR) peak was observed, which was more pronounced in the sample synthesized without polystyrene. The shape of the SPR peak is influenced by several factors, including the presence of an outer layer, which facilitates the delocalization of free electrons at the interface [28], and electron-phonon and phonon-phonon relaxation, which intensifies in nanoparticles smaller than 20 nm, resulting in peak broadening [29]. These factors likely contributed to the overall suppression and broadening of the SPR peak in my samples.

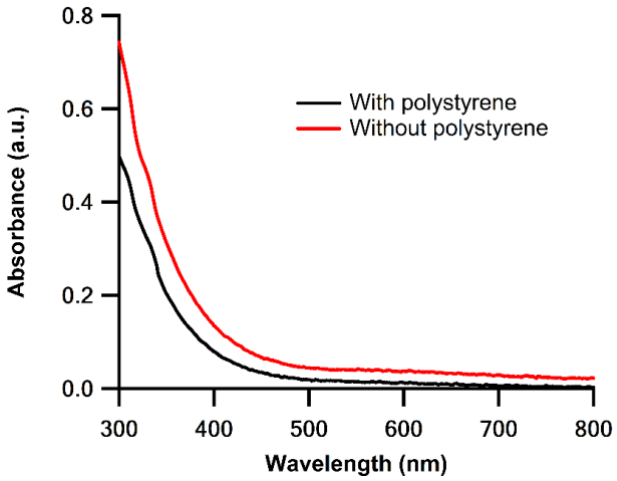

Figure 6. UV-Vis spectrum of carbon-encapsulated Au NCs in the presence and absence of polystyrene.

The TEM analysis and UV/Visible absorption spectra indicate that the carbon matrix not only influences the growth of NCs but also suppresses the SPR of the synthesized Au NCs. As a result, the carbon-encapsulated Au NCs exhibit no plasmonic properties, serving primarily as a support for carbon formation. However, achieving plasmonic properties in carbon-encapsulated Au NCs is essential, as it enhances their tunability and expands their potential applications in areas such as sensing, catalysis, and biomedical fields. In the context of PLAL,

various researchers have explored methods to induce plasmonic properties. For instance, reference 10 describes an approach where the SPR of Au NCs was restored by oxidizing the carbon layer. However, this process led to Au NC aggregation, preventing the maintenance of a consistent particle size even after oxidation. On the other hand, reference 13 reported the formation of ultrathin carbon layers, ranging from 0.6 to 2 nm, around Au particles through laser ablation in an ethanol/toluene mixed solution. However, the size of the inner noble metal was found to be less than 20 nm. Notably, neither study identified the most effective method for producing very small metal NCs with ultrathin carbon layers. Therefore, my experiment aimed to precisely control both the size of Au NCs and the thickness of the carbon layer by employing two strategies: adjusting the laser power and modifying the heat capacity of toluene.

Laser power effect on carbon-encapsulated Au NC size

Regulating the heat energy within the laser-ablated plasma plume is essential, as it directly impacts the energy transfer required for toluene decomposition. This means that adjusting the laser power allows for control over the carbon layer thickness. Accordingly, ablation experiments were conducted at four different laser power levels (104, 180, 350, and 550 mW) by altering the pulse current (Table 1). As illustrated in Figure 1, polystyrene plays a key role in minimizing particle size, enhancing dispersion, and preventing aggregation. To investigate this effect, the laser power was varied while maintaining a fixed polystyrene concentration of 50 mM.

The carbon layer thickness was analyzed using an extended Mie theory model for core-shell structures, where carbon serves as the outer shell and Au NCs form the core, as detailed in the experimental section. The results from TEM particle size analysis and carbon layer thickness measurements (Table 1) indicate that laser power significantly affects the thickness of the carbon layer surrounding the Au NCs. Lowering the laser power reduces the extent of solvent decomposition, leading to a thinner carbon layer. Notably, at very low power levels, particularly 104 mW, the Au NCs exhibited a slightly larger size. This is likely because, at reduced laser power, the heat generated by the plasma plume may not be sufficient to extensively decompose toluene molecules, resulting in slower carbon layer formation. This slower process provides more

Table 1 Primary particle diameter (determined via TEM analysis) of Au NCs prepared by PLAL under the presence of polystyrene (50 mM).

Laser power (mW)	Particle size (nm)	Carbon layer thickness (nm)
104	2.2 ± 0.4	2.4 ± 0.2
180	1.7 ± 0.2	3.0 ± 0.3
350	1.8 ± 0.4	3.5 ± 0.2
550	1.7 ± 0.3	4.2 ± 0.3

time for Au NCs to aggregate and grow, leading to increased particle size. Consequently, while 104 mW laser power is optimal for producing an ultrathin carbon layer, it presents challenges in controlling the size of Au NCs. On the other hand, at higher laser power, a thicker carbon layer effectively regulates the size of the Au NCs.

Figure 7(a) presents the UV-vis spectra of carbon-encapsulated Au NCs prepared under different laser power conditions. The data indicate that as the carbon layer thickness decreases at lower laser power, the quenching effect of SPR is reduced, allowing the plasmonic properties to emerge. A notable red shift in the SPR peak of Au NCs is observed compared to the typical peak at approximately 520 nm. This shift results from the high refractive index (n) of the carbon layer (n = 2.7) [30] in contrast to that of toluene (n = 1.5), which serves as the surrounding medium of the Au NCs [31].

Polystyrene concentration effect on carbon-encapsulated Au NC size

The second strategy focuses on regulating solvent decomposition by increasing the polystyrene concentration in the laser ablation medium. Since toluene has a relatively low heat capacity, it rapidly decomposes when subjected to the intense heat and pressure of the plasma plume. In contrast, polystyrene generally exhibits a higher heat capacity due to its molecular composition and greater molecular weight. Using differential scanning calorimetry, the heat capacities of toluene (1.1 ± 0.1 J/K), 200 mM polystyrene in toluene (4.6 ± 0.1 J/K), and 400 mM polystyrene in toluene (6.1 ± 0.2 J/K) were experimentally determined. These findings suggest that increasing the polystyrene concentration enhances the heat capacity of the system, thereby reducing toluene decomposition and minimizing the thickness of the carbon layer.

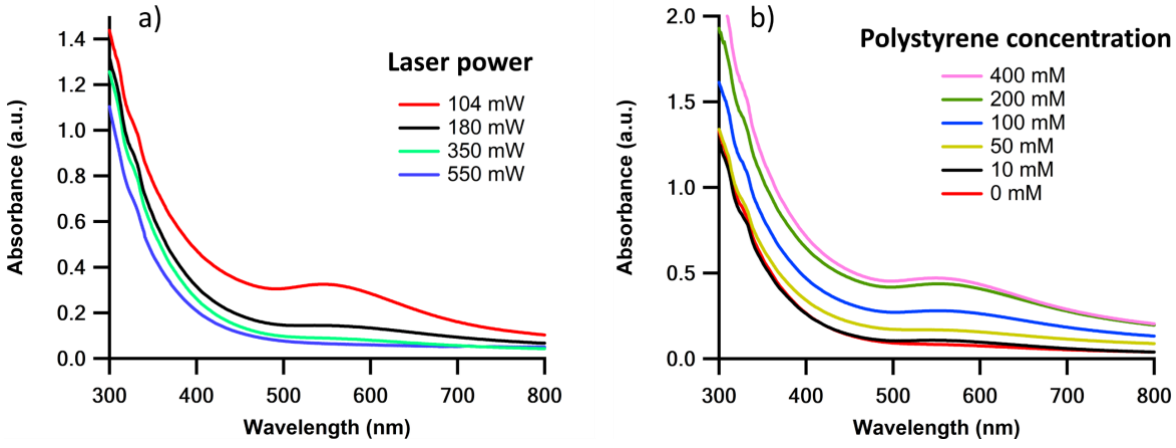

Figure 7. The UV-Vis spectrum of carbon-encapsulated Au NCs was obtained by using a) different laser powers in 50 mM polystyrene/toluene solution and b) different polystyrene concentrations by applying 104 mW average power. All the samples were prepared as 0.03 mM Au in THF.

Additionally, the presence of polystyrene facilitates the formation of smaller Au particles. Further laser ablation experiments conducted with varying polystyrene concentrations will provide additional insights into its effects. In this study, six different polystyrene concentrations (0, 10, 50, 100, 200, and 400 mM) were examined while maintaining a constant laser power of 104 mW, as previously applied.

Table 2 Results of PLAL on gold target in toluene under different concentrations of polystyrene. The average laser power was fixed to be 104 mW.

Polystyrene concentration (mM)	Particle size (nm)	Carbon layer thickness (nm)
0	2.8 ± 0.5	3.9 ± 0.4
10	2.5 ± 0.5	3.3 ± 0.4
50	2.2 ± 0.3	2.4 ± 0.2
100	1.7 ± 0.3	2.1 ± 0.2
200	1.7 ± 0.2	2.0 ± 0.3
400	1.7 ± 0.2	1.8 ± 0.2

The results presented in Table 2 clearly indicate that polystyrene concentration significantly impacts both the primary particle size of Au NCs and the thickness of the outer carbon layer. Specifically, as the polystyrene concentration increases, the Au NCs become smaller due to polystyrene acting as a stabilizer, preventing particle aggregation. Moreover, a higher polystyrene concentration reduces solvent decomposition, leading to a thinner carbon layer. This outcome further confirms that even under low-power laser irradiation, increasing the polystyrene concentration results in smaller Au NC sizes. Therefore, employing a low laser power with a high polystyrene concentration is an effective approach for obtaining small Au cores with thin carbon layers. The UV-vis spectra of Au NCs synthesized with different polystyrene concentrations are shown in Figure 7(b), illustrating that a thinner carbon layer reduces the SPR quenching effect. Consequently, this process enables the formation of carbon-encapsulated Au NCs with plasmonic properties.

Perspectives of MCL ablation

A PLAL experiment was performed using both the MCL and a higher-power ns-laser (Quanta-Ray PRO-250) under optimized polystyrene concentration (400 mM) to assess the MCL's effectiveness in producing a thinner carbon

Table 3 Results and PLAL parameters of the present MCL system and the ns-laser (Quanta-Ray PRO-250) system in a comparison experiment.

	Present MCL	Quanta-Ray PRO-250
Pulse energy (mJ)	1.3	25
Pulse duration (ns)	0.9	12
Spot diameter (μm)	130 ± 6	800 ± 13
Laser fluence (J/cm^2)	19.6	9.95
Repetition rate (Hz)	100	10
Particle size (nm)	1.7 ± 0.3	1.7 ± 0.3
SPR band	Present	Absent

layer, following the laser conditions specified in Table 3. The findings indicated that the SPR band was significantly suppressed for the Au NCs synthesized using the higher-power laser. In contrast, the Au NCs generated by the MCL system exhibited a distinct SPR band, as illustrated in Figure 8. This suppression is likely due to the formation of a thicker carbon layer, which results from the higher pulse energy of the Quanta-Ray PRO-250, attributed to its longer pulse duration. These results highlight the characteristic feature of the MCL, where the high-power laser-produced particles with a comparable size of 1.7 ± 0.3 nm to those obtained with the MCL, with a narrow particle size distribution. This outcome reflects the Quanta-Ray machine's laser fluence being half that of the MCL, which does not lead to a significant difference in particle size in the reported study [32].

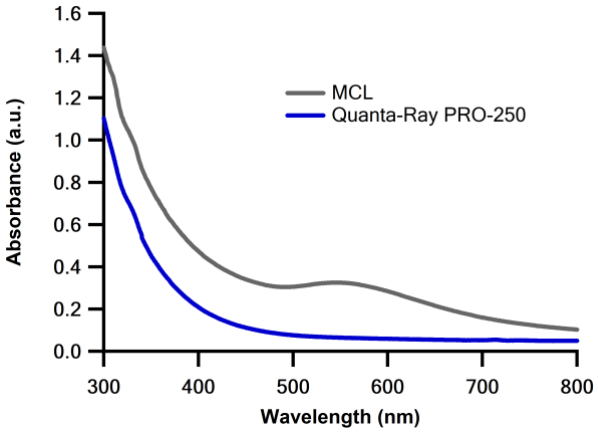

Figure 8. UV-Vis spectrum of carbon-encapsulated Au NPs prepared using the MCL system and Quanta-Ray PRO-250 laser in the presence of polystyrene (400 mM).

Photoluminescence properties of carbon-encapsulated Au NCs

Carbon nanomaterials have gained considerable attention as promising photoluminescent (PL) materials due to their potential applications [33,34]. This interest led us to explore the PL characteristics of carbon encapsulated within nanostructures generated by MCL. A key aspect of this study was analyzing how emission spectra vary with parameters such as excitation wavelength and carbon layer thickness. Initially, the excitation wavelength dependency of carbon-encapsulated Au NCs with the smallest Au cores and thinnest carbon layers was investigated. These nanostructures were synthesized using a laser power of 104 mW in a 400 mM polystyrene solution. To minimize interference from toluene and maintain consistent polymer concentrations across samples, the solvent was replaced with THF and excess polystyrene was removed via filtration after laser ablation. The PL response was examined across excitation wavelengths ranging from 350 nm to 450 nm. As illustrated in Figure 9(a), increasing the excitation wavelength resulted in a shift of emission peaks toward longer wavelengths. The most intense fluorescence emission was observed at an excitation wavelength of 330 nm. This confirms that the fluorescence spectra are excitation-dependent, a behavior commonly reported in luminescent carbon NPs, including carbon dots [33,34].

Subsequently, the PL spectra were analyzed for carbon layers of varying thickness while maintaining a constant Au NC size using the previously determined excitation wavelength of 330 nm. To eliminate interference from toluene, all samples were dissolved in THF, and excess polystyrene was removed post-laser ablation to standardize polymer concentrations. As shown in Figure 9(b), all samples displayed a primary emission peak near 410 nm with a shoulder peak around 510 nm. Notably, as the carbon layer thickness decreased, the intensity of the 410 nm emission peak progressively increased, whereas the 510 nm emission peak showed a slower increase. However, the peak positions remained unchanged across different samples, as no red or blue shifts were detected in the emission peaks, as seen in Figure 9(b) [35,36]. This suggests that the variations in sample size were not substantial enough to induce peak shifts.

PL intensity was quantified by maintaining a fixed Au NP concentration (0.03 mM). However, since fluorescence emission originates from the carbon material, it was essential to assess PL intensity under a constant carbon content. Experimentally determining the carbon

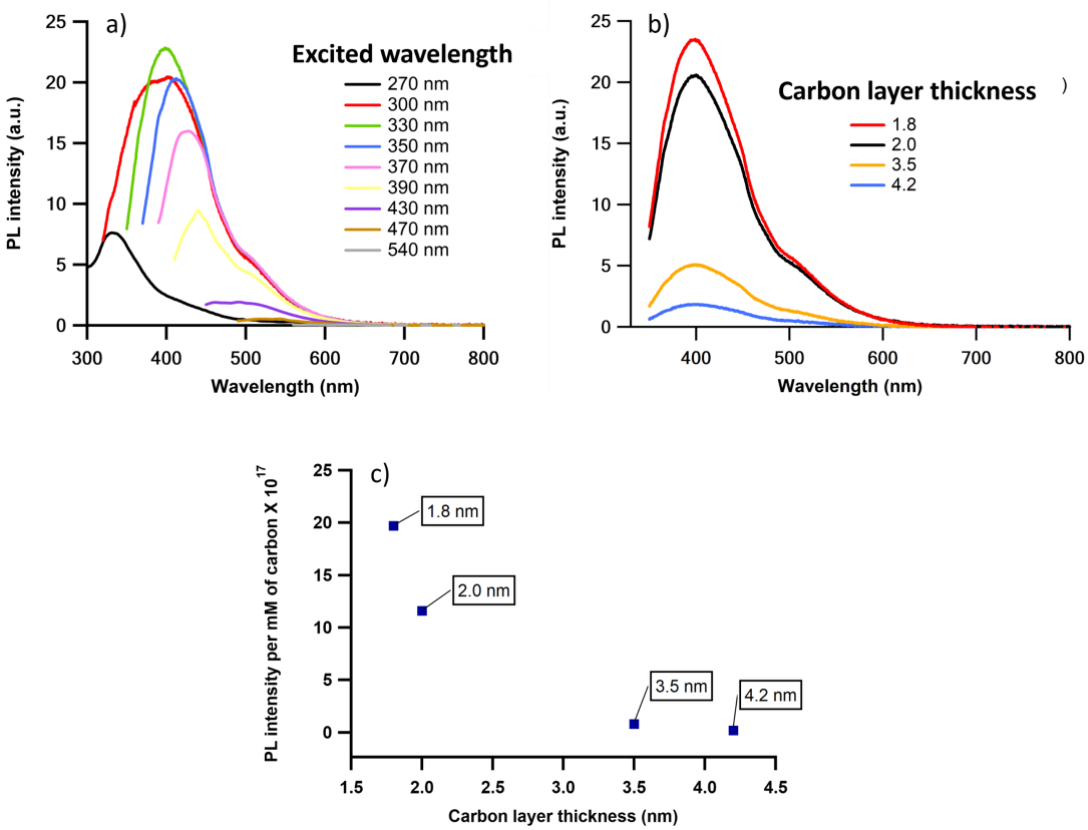

Figure 9. Emission properties of carbon-coated Au NCs were obtained by PLAL using MCL in a polystyrene/toluene mixture. a) Emission spectra of carbon-coated Au NCs excited at various wavelengths. b) Emission spectra of Au NCs with different carbon layer thicknesses. The excitation wavelength was 330 nm. c) Carbon layer thickness-PL intensity relationship. All the samples were prepared as 0.03 mM Au in THF.

content was challenging, so it was estimated based on the layer thickness for each sample. The emission intensities in Figure 9(b) were normalized by carbon content to evaluate PL intensity under fixed carbon conditions (Figure 9(c)). Consistent with Figure 9(b), decreasing the carbon layer thickness led to a gradual increase in the 410 nm emission peak intensity, following the same trend observed under fixed Au content. This demonstrates that the PL characteristics of carbon-encapsulated Au NCs can be significantly tuned by modifying the carbon layer thickness.

Regarding the fluorescence emission mechanism in carbon quantum dots, strong fluorescence is generally attributed to the radiative recombination of surface-confined electron-hole pairs [33,37]. In this case, the two fluorescence emissions observed at approximately 410 and 510 nm are likely linked to different excited states. The emission near 410 nm is speculated to originate from nano-sized sp2 carbon domains, corresponding to intrinsic state emission, whereas the longer-wavelength emission at 510 nm is associated with defect state emission caused by surface defects [38].

3-3. Conclusions

This study presents an innovative method for synthesizing carbon-encapsulated Au NCs using PLAL with the MCL system. By employing polystyrene as a stabilizing agent and toluene as a carbon source, the size of NPs and the thickness of the carbon layer can be controlled. Experimental findings indicate that polystyrene concentration significantly affects both the size of Au NCs and the carbon layer thickness. A lower laser power combined with a higher polystyrene concentration leads to the formation of smaller Au NCs with thinner carbon layers, demonstrating the efficiency of this technique. Additionally, the synthesized nanostructures exhibit enhanced photoluminescence properties, which are influenced by excitation wavelength and carbon layer thickness. This study provides a thorough analysis of the preparation and characterization of carbon-encapsulated metal NCs, emphasizing the advantages and potential applications of MCL-based PLAL techniques. The findings offer valuable insights into pulsed laser ablation in liquids, particularly regarding the influence of laser parameters and solvent properties on the process, contributing to the precise synthesis of advanced nanostructures.

3-4. Experimental Section

General

Bulk gold rod (99.99% purity), polystyrene (Sigma Aldrich), toluene (Merck Millipore), and tetrahydrofuran (THF) (Merck Millipore) were utilized. All chemicals were used as-is without further purification. Transmission electron microscopy (TEM) images were captured using a JEOL JEM-2100 electron microscope operated at 200 kV, with samples placed on a holey carbon support film-coated copper microgrid (EMJapan, U1003). Image analysis was performed using ImageJ software, and the mean diameter and standard deviation were calculated from an average of 300 particles. High-resolution TEM images for carbon-encapsulated Au NCs (prepared with 400 mM polystyrene, 104 mW laser power) were acquired using a Hitachi H-9000NAR microscope at 200 kV, again using a holey carbon support film-coated copper microgrid. To enhance contrast, a carbon coating was applied via spin-coating with reduced graphene oxide, which minimized the carbon layer's thickness on the copper grid. The carbon coating was performed following the reported method described in reference 39. The mean hydrodynamic diameter of the particles in toluene was measured via dynamic light scattering (DLS) using a Zetasizer Nano ZS (Malvern, UK) at a wavelength of 633 nm and a detection angle of 173°. Samples were sonicated for 15 min before the measurement. Measurements were averaged over at least three readings at 25°C. Raman spectra were recorded using a micro-Raman spectrometer (JASCO, NRS- 3100) with 532 nm excitation. A drop of the sample solution was dried on a Si wafer surface, and spectra were obtained by averaging 200 scans. For samples containing polystyrene, Raman analysis was performed on Au NPs encapsulated in carbon, prepared using 400 mM polystyrene and 104 mW laser power. The Au NC concentration was determined via inductively coupled plasma atomic emission spectroscopy (ICP-AES) using a Shimadzu ICPS-8100. Absorption spectra of the sample solutions were measured using a UV-Vis spectrometer (UV-3600, Shimadzu) with a 3.5 mL quartz cuvette. Photoluminescence emission spectra were recorded using a spectrofluorometer (RF-5031PC, Shimadzu) at various excitation wavelengths. For UV-Vis and photoluminescence measurements, excess polystyrene was removed by membrane filtration, and the solvent was replaced with THF. Heat capacity measurements were conducted using a differential scanning calorimeter (DSC) (STA 449C Jupiter, Netzsch) under a nitrogen atmosphere. Samples were sealed in aluminum pans, with an empty, hermetically sealed aluminum pan serving as the reference. The measurements were performed over a temperature range of 20°C to 80°C at a heating rate of 5°C/min. The DSC instrument was calibrated using a sapphire standard prior to the experiments.

General PLAL method

The gold target (5 × 15 mm) underwent cleaning by ultrasonication in acetone for 5 minutes, followed by rinsing with deionized water and drying before use. Subsequently, the target was affixed onto a custom-made holder (PEEK) equipped with a magnetic stir bar, and this assembly was positioned at the base of a Pyrex® vessel (30 × 80 mm). Zirconia beads (φ 6 mm) were placed between the vessel and the holder to stabilize the rotation axis. The liquid level was set to be 5 mm above the gold surface. Laser irradiation was focused directly on the target surface using an Nd:YAG/Cr^{4+}:YAG microchip laser. Additional specifications can be found in the cited papers.19,20 The initial laser condition to confirm the effect of polystyrene was conducted with a concentration of 50 mM and without polystyrene. Experiments were conducted under MCL parameters as follows: wavelength of 1064 nm, pulse energy of 1.8 mJ, pulse duration of 900 ps, peak power of >2 MW, and a repetition rate of 100 Hz, with an average power of 180 mW. Laser power effect experiments were carried out with 50 mM of polystyrene at different laser powers (104 mW, 180 mW, 350 mW, and 550 mW) by adjusting the laser current. Polystyrene concentration effect experiments were conducted with concentrations of 10, 50, 100, 200, and 400 mM, utilizing the following laser parameters: wavelength of 1064 nm, pulse energy of 1.0 mJ, pulse duration of 900 ps, peak power of >2 MW, and a repetition rate of 100 Hz, with an average power of 104 mW. Comparative experiments were performed with 400 mM polystyrene using an Nd:YAG laser (Quanta-Ray PRO-250) operating at wavelength, 1064 nm; pulse energy, 1500 mJ; pulse duration, 12 ns; peak power, 125 MW; average laser power, 15W; repetition rate, 10 Hz. In all experiments, the pulsed laser irradiation onto the gold target was conducted at room temperature for 60 minutes, stirring at 200 rpm.

Carbon Layer Thickness Determination

The carbon shell thickness of the Au NCs in Tables 1 and 2 was determined through Mie Theory fitting and applied to the UV-VIS spectra data in Figures 7 (a) and (b). Spectrum fitting was performed by using MATLAB, and the spectra were interpreted following the core-shell model as previously described by Amendola et al. [10].

Formula for Mie Theory calculations

Extended Mie theory was used to model light scattering and absorption for core-shell nanoparticles.

The polarizability $\alpha(\omega)$ of a core-shell sphere is described by the following equation [10,40]:

$$\alpha(\omega) = \frac{4\pi}{3}\,(R+d)^3\epsilon_0\,\frac{(\epsilon_s-\epsilon_m)\,(\epsilon+2\epsilon_m)+(\frac{R}{R+d})^3\,(\epsilon-\epsilon_s)\,(\epsilon_m+2\epsilon_s)}{(\epsilon_s+\epsilon_m)\,(\epsilon+\epsilon_s)+(\frac{R}{R+d})^3\,(\epsilon-\epsilon_s)\,(\epsilon_s-\epsilon_m)}$$

where R is the Au NC core radius, d is the carbon shell thickness, ϵ_0 is the vacuum permittivity, ϵ_s is the dielectric function of the carbon shell, ϵ is the dielectric function of the Au NC core, ϵ_m is the dielectric function of the surrounding medium (2.2) (here toluene) [41].

Extinction Cross-Section (σ_{ext}), reflecting the UV-vis absorption intensity, is calculated as:

$$\alpha_{ext}(\omega) = 4\pi k\ \mathrm{Im}[\alpha(\omega)]$$

where k is the wavenumber of the incident electromagnetic radiation.

The dielectric function $\varepsilon(\omega,R)$ for the Au NC core in the Mie theory model is given by:

$$\alpha(\omega,R) = \left[\epsilon_{1\,\infty}(\omega) + \frac{\omega_P^2}{\omega^2+\Gamma_\infty^2} - \frac{\omega_P^2}{\omega^2+\Gamma(R)^2}\right] + i[\epsilon_{2\,\infty}(\omega) + \frac{\omega_P^2\Gamma(R)}{\omega(\omega^2+\Gamma(R)^2)} - \frac{\omega_P^2\Gamma_\infty}{\omega(\omega^2+\Gamma_\infty^2)}]$$

where $\varepsilon_{1\infty}(\omega)$ and $\varepsilon_{2\infty}(\omega)$ are the real and imaginary components of the bulk dielectric function of Au. ω_P is the plasma frequency of gold (9 eV) [42]. Γ_∞ is the bulk metal's relaxation constant (0.07 eV). $\Gamma(R)$ is the size-dependent relaxation constant, which varies inversely with particle size [42].

The size-dependent relaxation constant $\Gamma(R)$ is calculated using:

$$\Gamma(R) = \Gamma_\infty + \frac{AV_F}{R}$$

Where V_F is the Fermi velocity of electrons in Au (1.4×10^6 m/s). A is a constant with a value near 1. R is the radius of the Au NC [42].

3-5. References

1. D. T. Tran, T. Kshetri, N. D. Chuong, J. Gautam, H. V. Hien, L. H. Tuan, N. H. Kim, J. H. Lee, *Nano Today*, **2018**, *22*, 100-131.
2. R. Kumar, K. Mondal, P. K. Panda, A. Kaushik, R. Abolhassani, R. Ahuja, H-G. Rubahn, Y. K. Mishra, *J. Mater. Chem. B*, **2020**, *8*, 8992-9027.
3. T. Zhang, H. Wang, X. Guo, S. Shao, L. Ding, A. Han, L. Wang, J. Liu, *Appl. Catal. B: Environ*, **2022**, *304*, 120925.
4. G. Li, H. Yang, H. Zhang, Z. Qi, M. Chen, W. Hu, L. Tian, R. Nie, W. Huang, *ACS Catal*., **2018**, *8*, 8396-8405.
5. X. Duan, J. Kang, W. Tian, H. Zhang, S. Ho, Y. Zhu, Z. Ao, H. Sun, S. Wang, *Appl. Catal. B: Environ*, **2019**, *256*, 117795.
6. W. Tian, H. Zhang, Z. Qian, T. Ouyang, H. Sun, J. Qin, M.O. Tadé, S. Wang, *Appl. Catal. B: Environ*, **2018**, *225*, 76-83.
7. M. Seipenbusch, A. Binder, *J. Phys. Chem. C*, **2009**, *113*, 20606-20610.
8. J. F. Li, Y. F. Huang, Y. Ding, Z. L. Yang, S. B. Li, X. S. Zhou, F. R. Fan, W. Zhang, Z. Y. Zhou, D. Y. Wu, *Nature*, **2010**, *464*, 392-395.
9. L. J. Gao, J. H. He, *J. Colloid Interface Sci*., **2013**, *400*, 24-30.
10. V. Amendola, G. A. Rizzi, S. Polizzi, M. Meneghetti, *J. Phys. Chem. B*, **2005**, *109*, 23125-23128.
11. D. Zhang, Z. Li and K. Sugioka, *J. Phys Photonics*, **2021**, 3, 042002.
12. D. Zhang, B. Gökce and S. Barcikowski, *Chem. Rev*., **2017**, 117, 3990-4103.
13. X. Xu, L. Gao, G. Duan, *Micromachines*, **2018**, *9*, 278.
14. E. Shiju, N. K. S. Narendran, D. N. Rao, K. Chandrasekharan, *Nano Express*, **2020**, *1*, 030026.
15. H. J. Jung, M. Y. Choi, *Appl. Surf. Sci*., **2018**, 457, 1050-1056.
16. J. F. Li, Y. J. Zhang, S. Y. Ding, R. Panneerselvam, Z. Q. Tian, *Chem. Rev*., **2017**, *117*, 5002-5069.
17. P. Munnik, P. E. de Jongh, K. P. de Jong, *Chem. Rev*., **2015**, *115*, 6687-6718.
18. B. S. Hettiarachchi, Y. Takaoka, Y. Uetake, Y. Yakiyama, H. H. Lim, T. Taira, M. Maruyama, Y. Mori, H. Y. Yoshikawa, H. Sakurai, *Ind. Chem. Mater.* **2024**, *2*, 340-347
19. B. S. Hettiarachchi, Y. Takaoka, Y. Uetake, Y. Yakiyama, H. Y. Yoshikawa, M. Maruyama, H. Sakurai, *Metals*, **2024**, ***14***, 155.

20. L. H. Sperling, Introduction to Physical Polymer Science; Wiley-Inter Science: New York, NY, USA, **1992**, p. 87.
21. F. Mafuné, J. Kohno, Y. Takeda, T. Kondow and H. Sawabe, *J. Phys. Chem. B*, **2001**, 105, 5114-5120.
22. H. Zhang, C. Liang, J. Liu, Z. Tian, G. Shao, *Carbon*, **2013**, 55, 108-115 23
23. C-Y. Shih, R. Streubel, J. Heberle, A. Letzel, M. V. Shugaev, C. Wu, M. Schmidt, B. Gökce, S. Barcikowski, L. V. Zhigilei, *Nanoscale*, **2018**, 10, 6900-6910.
24. C-Y. Shih, C. Wu, M. V. Shugaev, L. V. Zhigilei, *J. of Coll. and Inte Sci*., **2017**, 489, 3-17.
25. B. Bian, J. He, J. Du, W. Xia, J. Zhang, J. P. Liu, W. Li, C. Hu, A. Yan, *Nanoscale*, **2015**, 7, 975-980.
26. S. Reichenberger, G. Marzun, M. Muhler, S. Barcikowski, *ChemCatChem*, **2019**, 11, 4489.
27. T. C. Chieu, M. S. Dresselhaus, M. Endo, *Phys. ReV. B*, **1982**, 26, 5867- 5877.
28. A. Hernando, P. Crespo, M.A. Garcia, *The Scientific World JOURNAL*, **2005**, *5*, 972-1001.
29. S. Link, M. A. El-Sayed, *J. Phys. Chem. B*, **1999**, 103, 8410-8426.
30. X. Wang, Y. P. Chen, D. D. Nolte, *Optics Express*, **2008**, 26, 22105-22112.
31. H. Tyagi, J. Mohapatra, A. Kushwaha, M. Aslam, *ACS Applied Materials & Interfaces*, **2013**, *5*, 12268-12274.
32. K. A. Elsayed, H. Imam, M. A. Ahmed, R. Ramadan, *Optics & Laser Technology*, **2013**, 45, 495-502.
33. Y.-P. Sun, B. Zhou, Y. Lin, W. Wang, K. A. S. Fernando, P. Pathak, M. J. Meziani, B. A. Harruff, X. Wang, H. F. Wang, P. J. G. Luo, H. Yang, M. E. Kose, B. L. Chen, L. M. Veca, S. Y. Xie, *J. Am. Chem. Soc*., **2006**, *128*, 7756.
34. D. Y. Pan, J. C. Zhang, Z. Li, C. Wu, X. M. Yan, M. H. Wu, *Chem. Commun*., **2010**, *46*, 3681-3683.
35. L. Bao, Z. L. Zhang, Z. Q. Tian, L. Zhang, C. Liu, Y. Lin, B. Qi, D. W. Pang, *Adv. Mater*., **2011**, *23*, 5801-5806.
36. J. Lu, J. Yang, J. Wang, A. Lim, S. Wang, K. P. Loh, *ACS Nano*, **2009**, *3*, 2367.
37. L. Cao, X. Wang, M. J. Meziani, F. Lu, H. Wang, P. G. Luo, Y. Lin, B. A. Harruff, L. M. Veca, D. Murray, S.-Y. Xie, Y.-P. Sun, *J. Am. Chem. Soc*., **2007**, *129*, 11318.
38. F. Liu, M. H. Jang, H. D. Ha, J. H. Kim, Y. H. Cho, T. S. Seo, *Adv. Mater*., **2013**, *25*, 3657.

39. K. Yamada, M. Okamoto, M. Sakurai, T. Suenobu, K. Nakayama, *RSC Adv*., **2019**, *9*, 32940-32945.
40. U. Kreibig, M. Vollmer, Optical Properties of Metal Clusters; Springer-Verlag: Berlin, **1995**.
41. C. Rønne, K. Jensby, B. J. Loughnane, J. Fourkas, O. F. Nielsen, S. R. Keiding, *J. Chem. Phys*. **2000**, *113*, 3749-3756.
42. A. Derkachova, K. Kolwas, I. Demchenko, *Plasmonics*, **2016**, *11*, 941-951

Concluding Remarks

This comprehensive study has successfully demonstrated the potential of utilizing PLAL with the MCL system for the synthesis of Au NPs and carbon-encapsulated Au NPs. The portability and low power consumption of the MCL system make it a versatile tool for nanoparticle production across various solvent environments, both aqueous and organic.

In the aqueous medium, the study highlighted the significance of solution viscosity on the efficiency of Au NP ablation, influenced by the diffusion of gas bubbles formed during the process. The ability to produce small, consistent-sized Au NPs was linked to the short pulse duration (0.9 ns) and smaller spot size of the MCL system, which minimized the cavitation bubble size.

The study revealed that the thermal conductivity of the solvents and the incubation effect played significant roles in the productivity of Au NPs in organic solvents. High thermal conductivity solvents demonstrated enhanced ablation efficiency, while the vaporization enthalpy of the solvents influenced the process, especially in the absence of stabilizing polymers. These findings offer valuable insights into optimizing the NP synthesis process in various solvent environments, providing a pathway to overcome the limitations of high-power laser systems when handling flammable organic solvents.

Furthermore, the research introduced an innovative method for preparing carbon-encapsulated Au NCs in toluene using polystyrene as a stabilizing agent. The study demonstrated that adjusting laser power and polystyrene concentration effectively controlled the size of Au NCs and the thickness of the carbon layer. This approach also showcased enhanced photoluminescence properties of the synthesized nanostructures, dependent on excitation wavelength and carbon layer thickness.

Overall, this study provides a comprehensive understanding of the factors influencing PLAL in different media and establishes the potential of the MCL system in producing advanced nanostructures. The knowledge gained in this study on the pulsed laser ablation in liquids and the influence of laser parameters and solvent properties on the process will lead to the precise synthesis of new nanostructures, paving the way for further advancements in various fields, including materials science, nanotechnology, and chemistry.

List of Publications

1. Uncovering Gold Nanoparticle Synthesis using a Microchip Laser System through Pulsed Laser Ablation in Aqueous Solution
   Barana Sandakelum Hettiarachchi, Yusuke Takaoka, Yuta Uetake, Yumi Yakiyama*, Hwan Hong Lim, Takunori Taira, Mihoko Maruyama, Yusuke Mori, Hiroshi Y. Yoshikawa and Hidehiro Sakurai*
   Industrial Chemistry & Materials, 2024, *2*, 340-347
   DOI: 10.1039/d3im00090g

2. Mechanistic Study in Gold Nanoparticle Synthesis through Microchip Laser Ablation in Organic Solvents
   Barana Sandakelum Hettiarachchi, Yusuke Takaoka, Yuta Uetake, Yumi Yakiyama*, Hiroshi Y. Yoshikawa, Mihoko Maruyama and Hidehiro Sakurai*
   Metals, **2024**, *14(2)*, 155.
   DOI: 10.3390/met14020155

3. Tailoring Carbon-Encapsulated Gold Nanoclusters via Microchip Laser Ablation in Polystyrene Solution: Controlling Size, Structure, and Photoluminescent Properties
   Barana Sandakelum Hettiarachchi, Yumi Yakiyama* and Hidehiro Sakurai*
   RSC Applied Interfaces, **2025**, *2*, 772-779.

Acknowledgments

I sincerely appreciate Osaka University, the Japan International Cooperation Agency (JICA), and the Otsuka Foundation for permitting me to pursue my graduate studies at Osaka University and providing financial assistance throughout my studies.

I wish to express my sincere gratitude to my supervisor, Prof. Hidehiro Sakurai, for his exceptional supervision, mentorship, and guidance. This work would not have been successful without his critical insights and support in addressing the challenges encountered during my research.

I am also immensely grateful to Associate Prof. Yumi Yakiyama and Assistant Prof. Yuta Uetake for their unwavering teaching and guidance throughout my studies. Their assistance in preparing my thesis and manuscripts and their instructive comments and recommendations have been invaluable.

Moreover, I would like to extend my deep gratitude to all the professors and their students who supported me in various sample analyses.

Lastly, I want to thank the past and present members of the Sakurai laboratory for their constant support and assistance during experiments. All the members of the Sakurai laboratory have taught me a great deal during my time in the lab and my stay in Osaka, Japan.

I would also like to express my heartfelt appreciation to my family members and my wife, Bhagya Priyadarshani Kumari Wijesuriya, for their unwavering support and encouragement.

Finally, I dedicate this thesis to my mother, **Indrani Kumari Thilakarathna**, for her efforts.

March 2025

BARANA SANDAKELUM HETTIARACHCHI